POLITECNICO
MILANO 1863

SCUOLA DI INGEGNERIA INDUSTRIALE
E DELL'INFORMAZIONE

Fabrication of spin-orbit logic devices by thermal nanolithography

Tesi di Laurea Magistrale in
Physics Engineering - Ingegneria Fisica

Author: **Davide Bridarolli**

Student ID: 946904
Advisor: Prof. Christian Rinaldi
Co-advisors: Federico Fagiani, Matteo Cantoni
Academic Year: 2021-22

Abstract

The energy consumption of information and communication technology is increasing worldwide while silicon-based CMOS is approaching its scaling limit. Motivated by these trends, the investigation of next-generation non-volatile computing and memory devices in which data and logic coexist is vital. A remarkable pathway was suggested in 2018 by Intel in the article titled "Beyond CMOS computing with spin and polarization" [1]. They showed quantitively that the combination of spin currents and multiferroics is a master choice for attojoule-class logic gates. In 2019, they also proposed a conceptual logic element called magneto-electric spin-orbit (MESO) device [2]. In order to make this concept a reality, two major points must be tackled: (1) the integration on silicon of radically different materials with outstanding properties and (2) dimensional scaling of devices below 50 nm, to make the output signal significant. Therefore the objective of this thesis is the exploitation of a rather new lithographic technique called "thermal scanning probe lithography" (t-SPL) aiming at the realization of devices with minimum feature size below 50 nm. t-SPL uses a hot sharp tip to create nanometer-sized patterns. In contrast with e-beam lithography, the approach does not require vacuum and avoids damage from electrons which is crucial when working with delicate films. Furthermore, it allows to use heating to locally induce physical or chemical modifications at the nanoscale. t-SPL is capable of *in-situ* simultaneous pattering and imaging of layers and can achieve sub-10-nm resolution, although for such a resolution, very complex processes including hard masks depositions and etchings are required. Instead, in the easier resist-based approach the resolution is typically limited to an ultimate 100-120 nm and above. Here I want to push forward the resolution achievable with a standard resist-based approach by engineering the thickness of the resist to reach the desired feature size, while keeping the fabrication process relatively simple and non-invasive, which is also suitable for 2D materials. The results of this work put the ground for the realization of devices based on novel materials that become more energy efficient by scaling the minimum feature.

Keywords: thermal nanolithography, fabrication, processing, materials, spin-orbit logic

Abstract in lingua italiana

Il consumo di energia per infrastrutture informatiche per elaborare ed immagazzinare dati sta aumentando in tutto il mondo. Tuttavia il CMOS basato su silicio sta raggiungendo il limite di scalabilità. Questi trend richiamano alla necessità di una nuova generazione di dispositivi che combinino funzionalità di elaborazione e memoria. Una possibile strada è stata suggerita da Intel nel 2018 con l'articolo "Beyond CMOS computing with spin and polarization" [1]. Nel 2019 hanno anche proposto un concept per un innovativo elemento logico chiamato magneto-elettrico spin-orbita (*magneto-electric spin-orbit* MESO) [2]. Per rendere questa idea una realtà, due punti principali vanno affrontati: (1) l'integrazione su silicio di materiali radicalmente differenti dallo standard e (2) scalabilità dei dispositivi sotto i 50 nm, per rendere il segnale di uscita significativo. L'obbiettivo di questa tesi è stato quindi il raggiungere una scalabilità sotto i 50 nm con una tecnica relativamente nuova chiamata "litografia a sonda termica scansionante" (*thermal scanning probe lithography* t-SPL). t-SPL utilizza una punta scaldata per effetto Joule tramite il passaggio di una corrente estremamente affilata per creare pattern nanometrici. Al contrario della litografia elettronica, non ha bisogno del vuoto ed evita che i film sottili possano essere danneggiati da elettroni. Lo scambio di calore tra punta e campione può essere utilizzato anche per indurre cambiamenti fisici o chimici alla nanoscala. t-SPL permette la scrittura e la simultanea ispezione (*imaging*) di film sottili con risoluzione fin sotto i 10 nm. Tuttavia per raggiungere la risoluzione limite sono necessari dei processi complessi che comprendono deposizioni di maschere dure (*hard masks*) ed etching, che vanno oltre semplici processi standard basati solo su resist, solitamente limitati ad una risoluzione tra 100 e 120 nm. In questo lavoro vorrei spingere la risoluzione ottenibile con un processo standard basato su resist, mantenendo un processo semplice e poco invasivo, anche su materiali 2D costituiti da pochi strati atomici. I risultati di questo lavoro costituiscono una base per la realizzazione di dispositivi basati su materiali innovativi in cui l'efficienza energetica aumenta con la riduzione della dimensione minima.

Parole chiave: nanolitografia termica, fabbricazione, processi, materiali, logica spin-orbita

Contents

Abstract **i**

Abstract in lingua italiana **iii**

Contents **v**

Introduction **1**

1 Physics and devices **3**

1.1 Beyond CMOS with spin and polarization 3

1.1.1 Overview of the magneto electric spin orbit logic 3

1.1.2 Nanostructures for magnetic state readout 4

1.2 Spin dependent transport and electrical detection of spin currents 6

1.2.1 Two-current model and spin accumulation 6

1.2.2 Origin and phenomenology of the spin Hall effect 9

1.2.3 Analytical 1D spin diffusion model for the spin-to-charge conversion 18

1.3 The motivation behind this work 21

2 Methods **23**

2.1 Thin Film Deposition 23

2.1.1 Physical Vapour Deposition 23

2.2 Lithography 31

2.2.1 Thermal Scanning Probe Lithography 31

2.2.2 Optical Lithography 37

3 Fabrication **41**

3.1 The art of the Nanofrazor 42

3.1.1 Calibrations of the tips 42

3.1.2 Reading 45

3.1.3 Writing 46

3.1.4 Description of a complete lithographic process 50
3.2 The bilayer lift-off process 51
3.2.1 Details and optimization 53
3.2.2 Strategies to improve the resolution with a resist-based approach . . 57
3.2.3 Fabrication of the nanostructures 57

Conclusions and perspectives **63**

Bibliography **65**

List of Figures **71**

Acknowledgements **77**

Introduction

The energy consumption for information and communication technology infrastructures is constantly increasing and is predicted to reach 20% of the global energy consumption by 2030 [3]. This is due to the worldwide digitalization and the rise of technologies such as the Internet of Things (IoT), that drastically increase the volume of stored and processed data. The miniaturization of traditional silicon-based transistors is approaching its physical scaling limit, as the leakage currents become an issue as the channel length and the thickness of the gate dielectric is reduced to a few nanometers [4]. These trends call for architectures beyond the well-established CMOS platform, whose design and the scaling to tens of nanometres is beneficial in terms of energy efficiency. A lot can also be done in terms of architectures: a well-know source of power dissipation is caused by the enormous data shuttling between the information processing units (*e.g.* CPU) and memory in standard configurations, where the two are physically separated. This known as the the 'von Neumann bottleneck' for computing that significantly affects the energy efficiency, besides limiting the overall speed. It is nowadays accepted that a new generation of nanosized devices must intrinsically address this point with non-volatility, and the processing and memory must coexist in the same physical space in order to overcome the von Neumann scheme and ensure reduced power consumption. To allow for non-volatile, interconnected devices, four important ingredients are needed: state switching, state retention, state sensing and interconnects. Fig. 1 summarizes the wide variety of promising possibilities that are being investigated for beyond CMOS architectures in laboratories worldwide, spanning from photonics to exotic quasi-particles. Information storing in a material order parameter, such as ferromagnetism or ferroelectricity, could be solution for replacing or enhancing existing CMOS transistor, as suggested in 2018 by Intel [1]. In 2019, they also proposed a concept for a novel logic element called magneto-electric spin-orbit (MESO) device [2]. In order to meet the scaling requirements, ideally around and below 10 nm, for atto-joule class logic gates the thesis explored the nanofabrication of devices with an innovative lithographic technique: thermal scanning probe lithography (t-SPL). At the core of this innovative method of doing lithography there is an ultra-sharp heatable tip (similarly to that of an atomic force microscope) which is used for writing

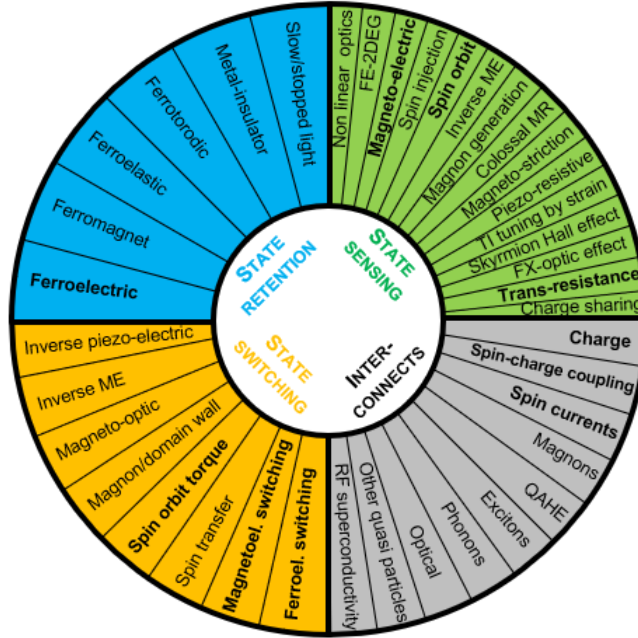

Figure 1: Beyond-CMOS "Wheel of technologies" for state retention, state sensing, state switching and interconnects

and simultaneously inspecting complex nanostructures. This approach, offers unique *in-situ* imaging and nanoscale patterning without ultra high vacuum in contrast to the more standard electron beam lithography (EBL). Moreover, the heat stimulus can be used to directly induce chemical (*e.g.* temperature-induced topological phase transition) and physical modifications (*e.g.* magnetic/ferroelectric domain manipulation) locally at the nanoscale which could open a new array of possibilities when working with novel materials.

The thesis is structured as follows:

Chapter 1 describes the MESO device in detail and the physical principles behind its operation.

Chapter 2 is an overview of the experimental techniques exploited in this work including t-SPL and deposition methods.

Chapter 3 describes the fabrication with t-SPL, employing a solely resist-based approach nominally limited to a minimum feature size of about 100-120 nm. The chapter will explain in detail how the process can be pushed close to 50 nm and below (in perspective), setting the ground for the development of spin-orbit based devices in Polifab.

1 | Physics and devices

This chapter will introduce the MESO device in detail, explaining its components and working principles. Then, an overview of the physical laws behind electrical spin-current injection (section 1.2) and spin-to-charge transduction is given. This will allow to better understand the motivations behind this thesis.

1.1. Beyond CMOS with spin and polarization

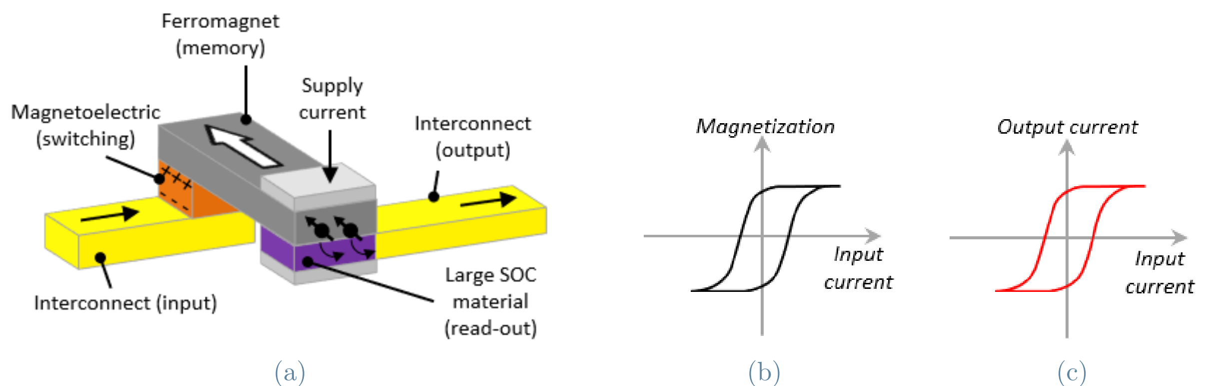

(a) (b) (c)

Figure 1.1: **(a)** MESO device formed with a magnetoelectric capacitor and a high SOC material stacked with a nanomagnet for state retention. The magnetoelectric transfer function in **(b)** shows how an input current can change the magnetization direction of the ferromagnet, displaying the typical hysteresis loop. The spin orbit transfer function in **(c)** shows the conversion of spin-to-charge.

1.1.1. Overview of the magneto electric spin orbit logic

The MESO device proposed by Intel (sketched in Fig. 1.1) includes a magnetoelectric switching capacitor, a ferromagnet and a spin-to-charge conversion module. The state retention is provided by a nanomagnet (FM), that can be switched by a magneto-electric (ME) capacitor. A suitable large spin-orbit coupling (SOC) material is used to transduce an injected spin current into an electrical one, allowing for readout of the magnetization

state by inverse spin-Hall effect (ISHE) [5] and the inverse Rashba-Edelstein effect (IREE) [6]. Techniques for sensing magnetic states in spintronics usually rely on measurements of magnetoresistances but they do not generate an electromotive force (*i.e.* a voltage) or a current that can be used to drive other circuit elements connected to them in cascade.

Furthermore, the integration of spin-textured ferroelectric Rashba semiconductors (FERSC)[7] enables a new proposal in the framework of spin-orbit logic. FERSC feature a complex k-dependent spin texture of the electronic bands in which the Kramers spin degeneracy is lifted [8]. The direction of the helical spin texture of the bands can be switched with the polarization through an external electric field [9]. This opens the possibility of obtaining a tunable spin-to-charge conversion module (FESO), which could reverse the output without the magnetoelectric capacitor. Fig. 1.2 shows a sketch of this concept proposed by C. Rinaldi *et al.*.

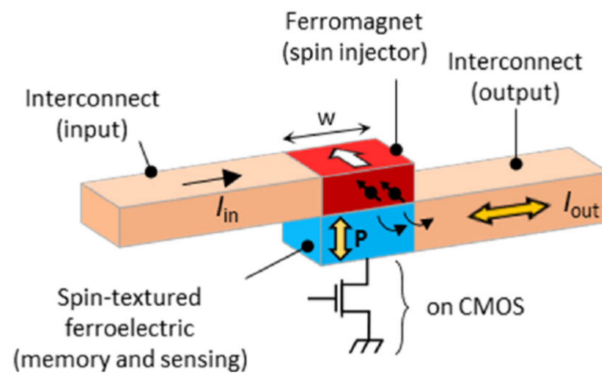

Figure 1.2: Ferroelectric spin-orbit logic (FESO) concept based on spin-textured ferroelectric stacks.

1.1.2. Nanostructures for magnetic state readout

The MESO and FESO concepts show promising results in the simulation but experimental demonstration of complete devices is still lacking. This chapter will present proof of concept spin-orbit transduction devices based on ferromagnet/heavy metal bi-layers [10]. In this thesis we tried to replicate such devices with t-SPL. The working principle is based on the conversion of input currents into output currents through spin-to-charge conversion (SCC) processes operated by a suitable material with large spin-orbit coupling. The transfer function from input to output gives the computing capability to those devices. If this transfer function can be stored in a non-volatile way in the device, then memory and computing functionalities reside in the same physical space, thus implementing the so-called logic-in-memory devices, holding potential for beyond-CMOS architectures (*e.g.*

MESO/FESO). A sketch of the device is depicted in Fig. 1.3. Starting from an electric current injection I_c^{app} in a ferromagnet (FM) electrode *(e.g.* CoFe or NiFe), a gradient of the electrochemical potential appears at the interface with a non-magnetic (NM) material (*e.g.* Pt or Ta), because of the different conductivities for minority and majority electrons. This gradient corresponds to a spin current I_s. In a pure spin current electrons with spin up and spin down are in equal number but flow in opposite directions. The injected spin current is then converted into a transversal electrical current I_c^{ISHE} by SCC conversion mechanisms (ISHE for heavy metals) taking place within the material (or materials stack) characterized by large spin-orbit coupling. The output of the device, which is a function of the magnetization m direction in the FM layer controlled by an external magnetic field $\vec{B}$, is represented by the by the output voltage V_{ISHE} generated in an open circuit condition by the charge accumulation. If we define the transverse resistance as $R_{ISHE} = V_{ISHE}/I_c^{app}$ where V_{ISHE} is the transverse measured voltage when I_c^{app} is injected in the FM, the spin Hall signal will be the difference in the resistance between the two magnetization orientations $2\Delta R_{ISHE}$. The physics behind this device will be explained in the following sections.

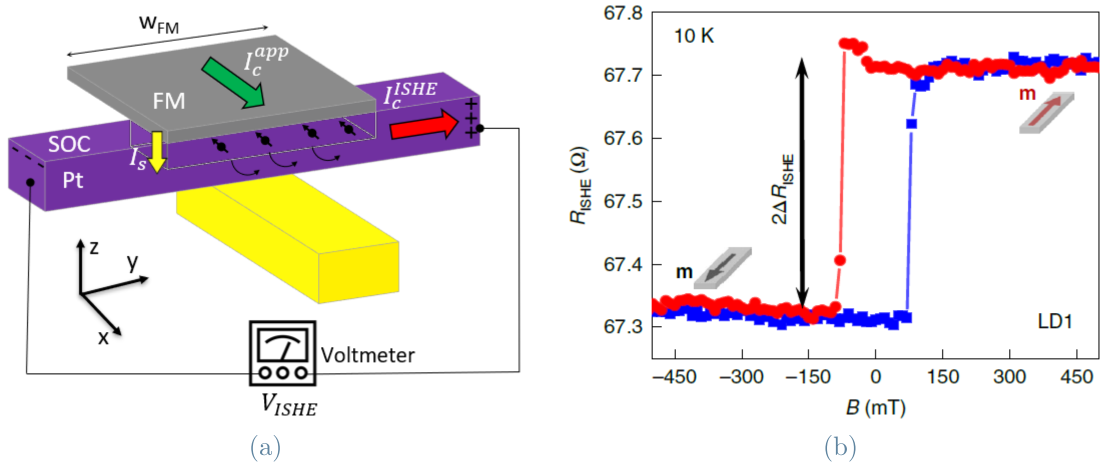

(a) (b)

Figure 1.3: **(a)** A ferromagnetic pillar (in grey) is patterned on top of a Pt nanostructure (in purple). A charge current I_c^{app} is applied to the nanomagnet (green arrow) in the x direction and it results in a spin current injection I_s along the z direction (yellow arrow) from the FM into Pt. The spin polarized current is converted into a charge current I_c^{ISHE} (red arrow) in the y direction by the ISHE in Pt, which results in a transversal charge accumulation that can be measured as a voltage (V_{ISHE}) in the open circuit condition. The portion of I_c^{app} that is not converted into I_s continues in the yellow electrode. **(b)** The plot shows the behavior of the signal $R_{ISHE} = V_{ISHE}/I^{app}$ as a function of the external magnetic field.

1.2. Spin dependent transport and electrical detection of spin currents

In order to understand the physics behind these devices, an introduction about the two-current model and the concepts of spin accumulation and spin currents is here reported. Then, an overview of the physical origin of the spin-to-charge conversion mechanism is given for spin-Hall effect in 3D systems and Rashba-Edelstein effect in 2D systems. At the end of the chapter the advantageous scaling law is demonstrated, being the motivation behind this work.

1.2.1. Two-current model and spin accumulation

Two-current model

The two-current conduction model initially proposed by Mott [11] provides a simple explanation for most of the electrical properties of transition metals. Fert and Campbell [12] applied this model to investigate the spin dependent transport in ferromagnetic materials Fe, Ni, Co and their alloys. The electric transport in ferromagnetic materials is mostly due to orbital-s electrons, whereas the electric resistivity is associated to the scattering processes suffered by the electrons between the s and d states, and during which the spin is conserved. Thus, in this model, the high resistivity of transition metals with partially filled d-states is explained by the dominant scattering of s electrons on the available d states. Moreover, the model supposes that the electrical current is carried by the spin up and spin down electrons in parallel. Denoting the electrical conductivities for majority and minority spin populations as $\sigma_\uparrow$ and $\sigma_\downarrow$, respectively, the application of the Drude's model for each spin channel leads to:

$$\sigma_\uparrow = \frac{e^2 n_\uparrow \tau_\uparrow}{m_e} = \alpha_F \sigma\uparrow \tag{1.1}$$

$$\sigma_\downarrow = \frac{e^2 n_\downarrow \tau_\downarrow}{m_e} = (1-\alpha_F)\sigma\downarrow \tag{1.2}$$

Where $n_{\uparrow/\downarrow}$ is the majority/minority electron density near the Fermi level, e is the electron charge and $m_e \sim m_0$ is the effective mass which in this case is the rest mass of the electron in the parabolic bands approximation $E_{\uparrow\downarrow}(k) = \frac{\hbar^2 k^2_{\uparrow\downarrow}}{2m_e}$ and $\tau_{\uparrow/\downarrow}$ are the scattering time constants related to the mean free path of the electrons $\lambda_{\uparrow/\downarrow} = v\tau_{\uparrow/\downarrow}$ where $v \sim v_F$ for conduction electrons.The dimensionless factor $0 \leq \alpha_F \leq 1$ takes into account the asymmetrical conductivity carried by each channel. Considering that the relevant mech-

anism of scattering in ferromagnets is from s bands to partially filled $3d$ bands, and the spin is conserved, majority electrons will experience an higher conductivity. This is because for transition metals the most relevant term in the Drude's conductivity expression is $\tau^{-1} \propto n_{\uparrow/\downarrow}$ and the majority d$\uparrow$ bands are completely occupied near the Fermi level $n_{d\uparrow}(E_F) \sim 0$. Whereas $n_{d\downarrow}(E_F) > 0$ so that minority electrons are more strongly scattered into heavy states of the d$\downarrow$ band for which the density of states is large. It follows that $\alpha_F \neq 0.5$ in ferromagnets. We can define the so called spin polarization:

$$p_F = \frac{\sigma_\uparrow - \sigma_\downarrow}{\sigma_\uparrow + \sigma_\downarrow} \tag{1.3}$$

Considering a 1D system, the current densities for each spin channel can be written by applying the Ohm's law:

$$J \uparrow = \frac{\sigma_\uparrow}{e}\frac{\partial \mu \uparrow}{\partial x} \tag{1.4}$$

$$J \downarrow = \frac{\sigma_\downarrow}{e}\frac{\partial \mu \downarrow}{\partial x} \tag{1.5}$$

where x is the direction of the current flow and $\mu_{\uparrow/\downarrow}$ the spin dependent electrochemical potentials. A charge current is associated to the flow of charges. In an unpolarized charge current the number of spin and down electrons is the same, and they flow in the same direction. Whereas, in a spin current the spin population is imbalanced. In a pure spin current the flow of charges of different spin is opposite and equal, hence the charge current is zero. One can write the spin current density as $J_s = J_\uparrow - J_\downarrow$ while the charge current density is $J_c = J_\uparrow + J_\downarrow$. In non-ferromagnetic materials, $p_F = 0$, so that in principle, at equilibrium, the spin current is zero. However, for a non-magnetic material under spin current injection from a ferromagnet, this is not the case anymore.

Spin accumulation and spin diffusion length

To describe the spin accumulation due to the different fluxes of majority and minority electrons at the interface between ferromagnet and non-magnetic material, the Valet-Fert model will be employed. Assuming that the mean free path of the electrons is much smaller than the spin diffusion length, the transport equations can be written in terms of macroscopic quantities as:

$$\frac{\partial \mu_{\uparrow/\downarrow}}{\partial x} = \frac{e}{\sigma_{\uparrow/\downarrow}} J_{\uparrow/\downarrow} \tag{1.6}$$

$$\frac{\partial^2(\mu_\uparrow - \mu_\downarrow)}{\partial x^2} = \frac{(\mu_\uparrow - \mu_\downarrow)}{\lambda_s^2} \tag{1.7}$$

Equation 1.2.1 is the Ohm's law applied for each spin channel and 1.7 is a diffusion equation. The spin diffusion length, which is defined as the average distance that electrons diffuse between spin-flipping collisions λ_s^2, might be different for each spin population. By combining these two differential equations one can get the general solution for the electrochemical potential:

$$\mu_{\uparrow/\downarrow} = (1 - p_F^2)\rho^* J_c x + k_1 \pm (1 \pm p_F)[k_2 e^{\frac{x}{\lambda_s}} + k_3 e^{-\frac{x}{\lambda_s}}] \tag{1.8}$$

where $\rho^* = \frac{\rho}{(1-p_F^2)}$ is the effective resistivity and k_1, k_2, k_3 are constants that depend on the boundary conditions, namely the continuity of the electrochemical potential at the interface and the conservation of charge and spin currents. The spin accumulation is defined as the the difference between the electrochemical potentials of majority and minority electrons, $\Delta\mu = \mu_\uparrow - \mu_\downarrow$. The 1-dimensional solution of the diffusion equation 1.7 for the spin accumulation is:

$$\Delta\mu = Ae^{-\frac{x}{\lambda_s}} + Be^{\frac{x}{\lambda_s}} \tag{1.9}$$

With A and B depend on the boundary conditions.

Application Of the Valet-Fert model

In this section the Valet-Fert model will be applied to describe the spin accumulation and spin current at the vicinity of a simple ferromagnetic/non-magnetic (F/N) interface, as shown in Fig. 1.4. In the ferromagnet $J_\uparrow > J_\downarrow$ whereas $J_\uparrow = J_\downarrow$ in the non-magnetic material: this mismatch leads to a non-equilibrium spin accumulation in the vicinity of the F/N interface which is directly related to the difference of the electrochemical potentials. The spin polarization of the current injected from the ferromagnet will decrease during its propagation in the medium, until the equilibrium state of spin up and spin down electrons is reached far from the interface, with a polarization equal to p_F in the ferromagnet and equal to zero in the non-magnet.

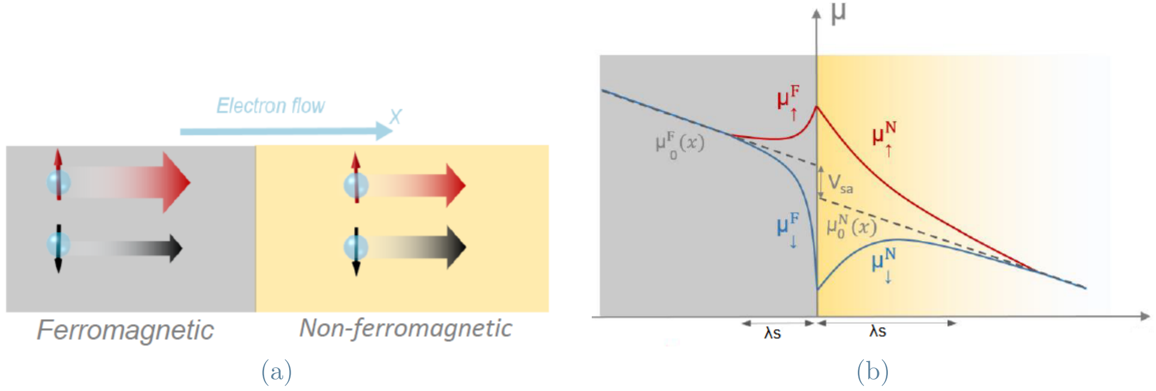

Figure 1.4: **(a)** Schematic representation of the current in a F/N junction. The red and black arrows denote the conductivities for up and down spin electrons far from the interface. In the ferromagnetic material majority electrons experience less scattering events than minority, this leads to an higher majority current. **(b)** Electrochemical potential landscape at the F/N interface. Here, the red and blue lines represent the electrochemical potentials for the majority and minority spin populations. The transition from the ferromagnet to the non-magnet results in a spin current injection and a voltage drop at the interface V_{ac}, due to the spin accumulation.

1.2.2. Origin and phenomenology of the spin Hall effect

Spin-orbit coupling

The Maxwell's equations employ the so called Lorentz transformations of frame of reference, which are given by special relativity. Thus, a change of frame can transform an electric field into a magnetic field, and vice-versa; this means that an electron moving in the laboratory frame at a velocity non-negligible with respect to the speed of light in an electric field, will experience in its own frame, a magnetic field. The electric field therefore transforms into a relativistic magnetic field which can interact with the spin angular momentum of the particle.

This physical phenomenon is the so-called spin-orbit coupling (SOC), and helps in explaining degeneracy lifts in the fine structure of the hydrogen atom, molecules or solid bands. If the non-relativistic equation of the electron is applied in electron band-structure calculations, the relativistic term can be added as a perturbation to the Hamiltonian. In other words, from the comparison between the non-relativistic Schrodinger equation and the relativistic Dirac equation, emerges an additional term due to the SOC which leads to spin up and spin down states splitting.

Effect of SOC in atoms

In order to approach the physics of SOC, let's first consider the problem of an electron moving in an atomic potential treated as a classical field. The non-relativistic Hamiltonian is:

$$\hat{H}_0 = \frac{\hat{p}^2}{2m_e} + V(r) \tag{1.10}$$

where $\hat{p} = -i\hbar\nabla = -i\hbar(\frac{\partial}{\partial x}\vec{\imath} + \frac{\partial}{\partial y}\vec{\jmath} + \frac{\partial}{\partial z}\vec{k})$ is the momentum operator, m_e is the rest mass of the electron and $V(r)$ is the potential. Let us now consider an electron moving in the atom frame, where there is no magnetic field. The relativistic perturbation of the Hamiltonian can be added:

$$\hat{H} = \hat{H}_0 + \Delta H \tag{1.11}$$

The correction term can be deduced from the classical Joules-Bernoulli equation, when considering this relativistic transformation of two inertial frames (the nuclear frame to the electron frame), the electron in its frame experiences the electric field $\vec{E}$ due to the nuclei as an effective magnetic field $\vec{B}$[13]:

$$\vec{B} = \gamma(\vec{B_0} - \frac{1}{c^2}\vec{v} \times \vec{E}) \tag{1.12}$$

Where $\vec{B_0} = 0$ is the actual magnetic field of the nuclei, $\vec{v}$ is the relative speed between the two frames of references and $\gamma = 1/\sqrt{1 - \frac{v^2}{c^2}}$ is the Lorentz factor. The effective SO magnetic field is therefore:

$$\vec{B}_{SO} = -\gamma\frac{1}{c^2}\vec{v} \times \vec{E} \tag{1.13}$$

where $\vec{E} = -\nabla V$ which can be written in radial coordinates as $\vec{E} = -\frac{\vec{r}}{|r|}\frac{\partial V(r)}{\partial r}$ and v can be written as $\frac{p}{m_e}$, the SO field is:

$$\vec{B}_{SO} = \gamma\frac{1}{m_e c^2}\frac{dV}{dr}\frac{1}{r}\vec{r} \times \vec{p} = \gamma\frac{1}{m_e c^2}\frac{dV}{dr}\frac{1}{r}\vec{L} \tag{1.14}$$

Where L is the orbital angular momentum. As the treatment of the problem has been carried out in a semi-classical approach with the Schrödinger equation; one has to artificially add the hypothesis that the electron possesses a magnetic moment due to its spin:

$$\vec{\mu}_S = -g_s\mu_B\frac{\vec{S}}{\hbar} \tag{1.15}$$

Where S is the spin angular momentum vector, g_s is the Landé factor and μ_B is the Bohr magneton; this term would be already included within the relativistic Dirac equation. The

perturbation to the Hamiltonian in this picture is defined as the coupling of the effective value of relativistic $\vec{B}$ field and spin and can be simply seen as the Zeeman effect [14]:

$$\Delta H = -\vec{\mu}_s \cdot \vec{B}_{SO} \tag{1.16}$$

The correction is thus:

$$\Delta H = \frac{\mu_B \gamma g_s}{\hbar m_e c^2} \frac{1}{r} \frac{dV}{dr} \vec{L} \cdot \vec{S} \tag{1.17}$$

It can be demonstrated that an additional term has to be added due to the Thomas precession [15], which takes into account the change in the spin precession frequency when changing the frame of reference:

$$\Delta H_T = -\frac{\mu_B \gamma g_s}{2\hbar m_e c^2} \frac{1}{r} \frac{dV}{dr} \vec{L} \cdot \vec{S} \tag{1.18}$$

Finally, the total spin–orbit Hamiltonian can be written:

$$\Delta H_{SO} = \Delta H + \Delta H_T = \frac{\mu_B \gamma g_s}{2\hbar m_e c^2} \frac{1}{r} \frac{dV}{dr} \vec{L} \cdot \vec{S} \tag{1.19}$$

$\gamma \sim 1$ at low speeds and $g_s \sim 2$, and $\mu_B = \frac{e\hbar}{2m_e}$. The SOC hamiltonian is [14]:

$$\Delta H_{SO} = \frac{e}{2\hbar m_e^2 c^2 r} \frac{dV}{dr} \vec{L} \cdot \vec{S} \tag{1.20}$$

Phenomenology of the spin Hall effect

The phenomenology of spin Hall effect (SHE) and other spin-dependent effects are shown in Fig. 1.5. The SHE has been theoretically predicted by M.I. Dyakonov and V.I. Perel in 1971 [17]. The principle of SHE can be summarized as follows: an applied charge current produces a transverse pure spin current, that is, up-spin and down-spin electrons moving oppositely in the transverse direction; the appearance of a pure spin current will induce spin accumulations of opposite sign at the edges of the samples, even in a non-magnetic material where the spin polarization is equal to zero[16][5]. Viceversa, when a pure spin current is injected in a non-magnetic sample with high SOC, the inverse spin Hall effect (ISHE) can be observed: the spin current it's converted in a transverse charge current, orthogonal to both the spin direction and the electric current [16][5]. No external magnetic field is required to observe the SHE or the ISHE.

In magnetic materials there's an imbalance between spin up and spin down electrons that leads to a non-compensated charge accumulation at the edges of the sample: this effect

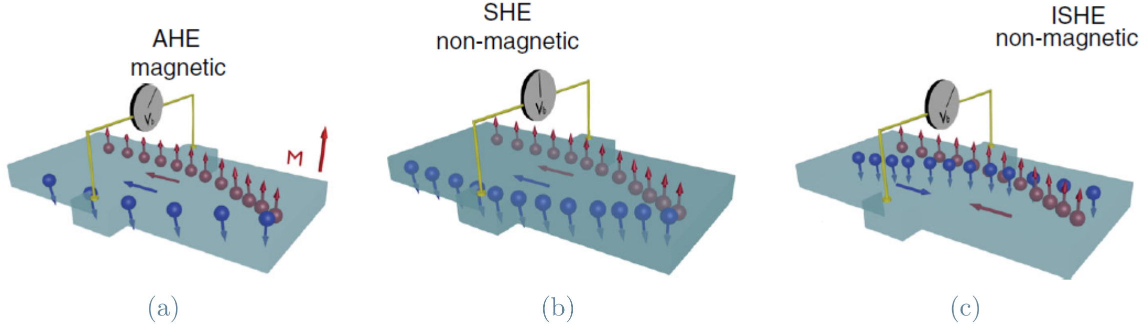

(a) (b) (c)

Figure 1.5: An illustration of every spin-dependent Hall effect. The spin up and spin down carriers are shown in red and blue. **(a)** In the AHE, a charge current flowing in a ferromagnetic material generates a polarized transverse charge current. **(b)** In the SHE, a charge current generates a transverse polarized pure spin current. **(c)** In the ISHE, a pure spin current generates a transverse charge current. As we can see every effect exhibit the same spatial symmetry. Adapted from [16].

is called anomalous Hall effect (AHE)[18]. A transverse voltage related to AHE can be easily measured in ferromagnets [19].

In order to give a physical description of the coupling between charge and spin currents due to SHE, the starting point is the drift diffusion equation for charge currents, which is given by [17][20]:

$$\frac{\vec{J_c}}{e} = \mu n \vec{E} + D\nabla n \tag{1.21}$$

where $J_c = J_\downarrow + J_\uparrow$, μ is the electron mobility, $\vec{E}$ is the electric field, n is the conduction electron density, and D is the electron diffusion constant. The mobility and the diffusion constants are related by the Einstein relation: $D = \mu k_B T$ where k_B is the Boltzmann's constant and T is the temperature. Similarly, one can define a drift diffusion equation for the spin current tensor $J^s_{i,j}$, where each element in the tensor denotes a current flowing in the i direction with spin polarization along j [17][20]:

$$\frac{J^s_{i,j}}{\hbar} = -\mu n E_i P_j + D\frac{\partial P_j}{\partial x_j} \tag{1.22}$$

The SHE stems from the coupling between charge and spin currents due to the spin-orbit interactions. This coupling is introduced as follows [17][20]:

$$\frac{\vec{J_c}}{e} = \mu n \vec{E} + D\nabla n + \Theta_{SH}\mu(\vec{E} \times \vec{P}) + \Theta_{SH} D(\nabla \times \vec{P}) \tag{1.23}$$

$$\frac{J^s_{i,j}}{e} = -\mu n E_i P_j + D\frac{\partial P_j}{\partial x_j} - \epsilon_{ijk}\Theta_{SH}(\mu n E_k + D\frac{\partial n}{\partial x_k}) \tag{1.24}$$

Where ϵ_{ijk} is the unit antisymmetric tensor and Θ_{SH} is the spin-Hall angle which is a material figure of merit determining the conversion rate between charge and spin currents. The third term in 1.24 describes the direct SHE, where a transverse spin current is generated in response to an electric field. Similarly, the third term in 1.23 represents the AHE in the presence of a net spin polarization typical of ferromagnets, while the fourth term describes the ISHE, i.e., the generation of a charge current in response to gradient in the spin accumulation. Note that thermal gradients and other possible sources for currents can be included in 1.23 and 1.24, however they will be neglected because at this point there are no conclusive experiments showing them [21]. The polarization density has to satisfy the continuity equation:

$$\frac{\partial P_j}{\partial t} + \frac{\partial J^s_{ij}}{\partial x_i} + \frac{P_j}{\tau_s} = 0 \tag{1.25}$$

where τ_s is the spin relaxation time. If we consider for simplicity a collinear model in which the spins are polarized along only one direction, it becomes possible to define a vector, rather than using a tensor, for the spin current density $\vec{J}_s$. In this framework, let's consider now an applied current along the y direction with a spin polarization along the x direction, the diffusion equation for the spin current in SHE becomes:

$$\frac{J^s_z}{e} = -\Theta_{SH}\epsilon_x \mu n E_y \tag{1.26}$$

$$J^s_z = \Theta_{SH}\epsilon_x J_y \tag{1.27}$$

and in the general case:

$$\vec{J}_s = \Theta_{SH}\vec{J}_c \times \vec{s} \tag{1.28}$$

Where s is the direction of the spin polarization. In the same way, the expression of the charge current in ISHE can be written as:

$$\vec{J}_c = \Theta_{SH}\vec{J}_s \times \vec{s} \tag{1.29}$$

Microscopic mechanism of SHE

Being $\sigma^c_{xx} = ne\mu$ the longitudinal charge conductivity and $\sigma^s_{xy} = n\hbar\mu\Theta_{SH}$ the spin Hall conductivity, which define the charge and spin current responses to an electric field re-

spectively one can easily see that the spin Hall angle is:

$$\Theta_{SH} = \frac{\sigma^s_{xy}}{\sigma^c_{xx}} \frac{e}{\hbar} \tag{1.30}$$

The spin Hall angle is the most important parameter of the SHE material. A quantitative theoretical description of the spin Hall conductivity and can be obtained by considering the microscopic mechanisms discussed below. There are different mechanisms that may give rise to spin Hall effects: extrinsic effects (e.g. spin skew scattering and side jump scattering), and intrinsic contributions from the band structure itself. Jin *et al.* [22] suggested an empirical relation in which the different contributions in the anomalous Hall conductivity are separated by their scaling with the temperature dependence of the charge conductivity. The experimental relation that they found is:

$$\sigma^s_{xy} = -(\frac{\alpha}{\sigma_{xx0}} + \frac{\beta}{\sigma^2_{xx0}})\sigma^2_{xx} - b \tag{1.31}$$

where σ_{xx0} is the residual impurity contribution to the charge conductivity at low temperatures, α, β and b are fitting parameters which are possibly related to the skew scattering, side jump and intrinsic contributions to the anomalous Hall conductivity, respectively. Recent theoretical calculations by Shitade and Nagaosa support the validity of this scaling behavior for the anomalous Hall conductivity [23].

Extrinsic Effects

Extrinsic mechanisms are possible explanations for the anomalous spin Hall conductivity, where spins acquire a transverse velocity due to spin-orbit coupling during the scattering of electrons. This is somewhat confusing, because the source of the scattering can have both extrinsic (*e.g.*, impurities and grain boundaries), as well as intrinsic (*e.g.*, phonons) origins. Extrinsic effects divide in spin skew scattering and side-jump scattering.

1. *Spin Skew Scattering*: Spin skew scattering (figure 1.6a), also known as Mott scattering [24], is an effect in which the spin-orbit coupling in the scattering centers creates an effective magnetic field gradient within the scattering plane. This field gradient results in a net force toward or away from the scattering center, depending on the direction of the spin of the carrier. Thus, the direction of the electron momentum after scattering becomes spin-dependent and this gives rise to spin Hall effects even for isotropic scattering in the presence of spin-orbit interactions, and there is no need for additional symmetry breaking. The wave vector is not conserved during the scattering event. The contribution to the spin Hall conductivity from skew scat-

tering is directly proportional to the longitudinal conductivity, which means that the spin Hall angle defined in 1.30, is independent of the impurity concentration but depends on the contrast between the spin-orbit coupling of the impurity and the host [25].

2. *Side-Jump Scattering*: During side-jump scattering (figure 1.6b) the carriers acquire a spin-dependent acceleration and deceleration, which results in an effective transverse displacement upon repeated scattering [26]. Therefore, also side-jump scattering occurs at the impurity site, but in this case the electron wave vector is conserved. The contribution to the spin Hall conductivity due to side-jump scattering results in a spin Hall angle proportional to the impurity concentration because $\sigma_{SJ} \propto \sigma_{imp}^2$ [27]. This contribution to the SHE is usually smaller than the skew scattering one, but at high enough impurity concentrations it may become dominant [27].

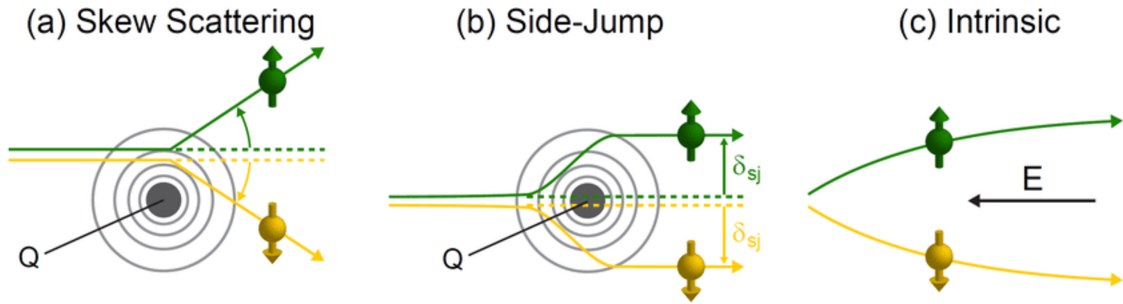

Figure 1.6: **(a)** Spin dependent skew scattering. Carriers with different spins (green and yellow colours) are deflected in the opposite way by the gradient in the relativistic magnetic field near an atom, the wave-vector is not conserved. **(b)** side-jump scattering, the wave-vector is conserved in this case. **(c)** Intrinsic SHE in which the spin dependent displacement is caused by asymmetries in the electronic band structure.

Intrinsic effects

Intrinsic spin Hall effects refer to systems where the transverse spin dependent velocities originate from spin-orbit splitting of the electronic band structure. Thus, in contrast to extrinsic effects, the transverse spin current is generated in between scattering events, instead of during the scattering. The theoretical framework behind these intrinsic effects has been recently formulated in terms of Berry curvature $\Omega_n^z(\vec{k})$ [28]. Without entering into detail here, the Berry curvature is determined by the presence of virtual interband transitions. This contribution to the spin Hall conductivity is dominant in those parts of the band structure where degenerate bands are split by spin-orbit interactions, and the

Fermi level is located in this gap. The Berry curvature is opposite for the bands on either side of the spin-orbit split gap. Therefore, it can be demonstrated that the intrinsic spin Hall conductivity is proportional to the spin-orbit polarization at the Fermi level [29]:

$$\sigma^s_{xy} \approx \frac{e}{4a}\frac{\langle l \cdot s\rangle_{FS}}{\hbar^2} \tag{1.32}$$

with a being the lattice constant. For example, in the case of Pt and Pd, this effect is due to the spin-orbit splitting of the degenerate d-bands at the L and X points near the Fermi level. Following Hund's rules, in transition metals the spin Hall conductivity is expected to be positive for more than half-filled d-bands and negative for less then half-filled. Calculations based on the tight binding model verified this hypothesis [28]. Picture 1.7 shows the intrinsic spin Hall conductivity for several 4d and 5d transition metals.

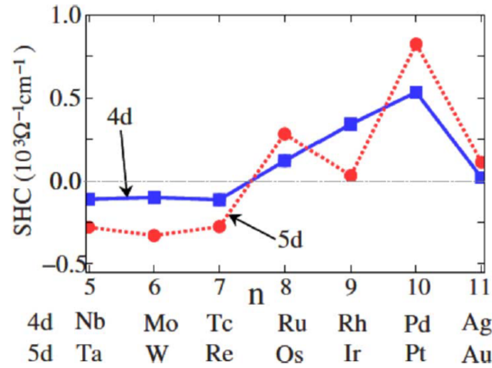

Figure 1.7: Intrinsic spin Hall conductivity calculated with tight binding for different 4d and 5d transition metals. Adapted from [28].

Intrinsic effects from symmetry breaking

Without entering into detail on this topic, it should be pointed out that aside from intrinsic spin Hall effects in the bulk of transition metals, it is also possible to have intrinsic spin Hall effects due to spin-orbit coupling arising from the symmetry breaking. The symmetries of a crystal can include the time-reversal symmetry ($\psi(t) = \psi(-t)$) and the inversion symmetry ($H(r) = H(-r)$). If both these symmetries are present it follows that the eigenvalues satisfy the condition $E(k, \uparrow) = E(k, \downarrow)$, where k denotes the electron wave-vector, and $\uparrow$ / $\downarrow$ corresponds to the spin direction. If only the time reversal symmetry is present the condition becomes: $E(k, \uparrow) = E(-k, \downarrow)$. In crystals with broken space-inversion symmetry, the electronic bands are spin-split, and the spin direction is momentum dependent as determined by the spin–orbit field. This is caused by the presence of a gradient in the electrostatic potential of the lattice/unit cell that results

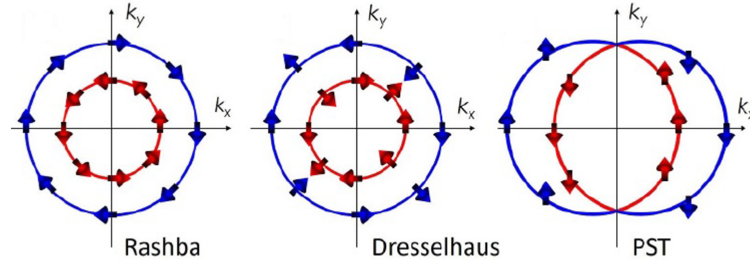

Figure 1.8: Blue and red arrows indicate spin orientation for the two SOC-split bands at the Fermi level. The spin textures can be of three different types: Rashba,Dresselhaus, and PST. Adapted from [8].

in a field that couples to the electron spin through the intra-atomic SOC. The inversion asymmetry in crystals can for instance be obtained in bulk semiconductor compounds with cubic zinc blende lattices as was first demonstrated by Dresselhaus for zinc-blende structure crystals [30]. He demonstrated that the first non-vanishing term in the SOC expansion for materials of this crystal symmetry is cubic in wave vector $\vec{k}$. It was predicted later that the SOC linear in wave vector $\vec{k}$ exists in the bulk wurtzite structure and two-dimensional (2D) electron gases, this is now referred to as the Rashba effect. The Rashba effect has been observed at surfaces and interfaces [31], bulk polar semiconductors [32] and 2D materials [33]. The spin–momentum coupling linear in k can also lead to the linear Dresselhaus SOC. Among non-centrosymmetric materials exhibiting the Rashba and Dresselhaus effects are ferroelectrics. Ferroelectrics are characterized by a spontaneous electrical polarization which is their order parameter, analogously to magnetization in ferromagnets. This polarization breaks the inversion symmetry and is switchable by an electric field, allowing for a tunable SOC. Both the SOC parameters and the direction of the helical spin texture in Rashba and Dresselhaus materials switch with polarization reversal. This behavior was experimentally verified in bulk GeTe [7] [9]. The typical spin texture of these materials is shown in Fig. 1.8. This materials exhibit tunable SCC conversion thorugh the inverse Rashba-Edelstein effect. It can be demonstrated that the relation between spin current density (per unit area) and charge current (per unit width) in a two-dimensional Rashba electron gas is given by:

$$J_x^c = \lambda_{IREE} J_y^s \tag{1.33}$$

where $\lambda_{IREE} = \alpha_R \tau / \hbar$ is the figure of merit for these materials. α_R is the Rasha coefficient and τ is the mean scattering time.

Ferroelectrics provide a promising platform to explore the coupling between spin, orbital,

valley, and lattice degrees of freedoms in solids and pave the way for nonvolatile spintronic devices, such as the Magneto Electric Spin Orbit logic.

1.2.3. Analytical 1D spin diffusion model for the spin-to-charge conversion

In order to show how these devices deliver a convenient scaling law, a one-dimensional spin diffusion model will be applied [34]. Consider the reference system in Fig. 1.9, if a

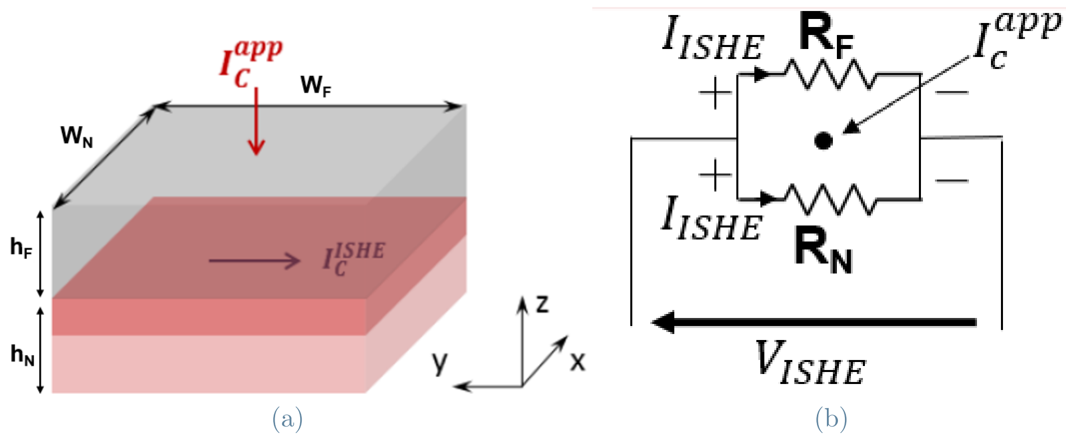

(a) (b)

Figure 1.9: **(a)** The image shows the heavy metal (*e.g.* Pt or Ta) /nanomagnet (*e.g.* CoFeB or NiFe) stack and the distribution of the currents. When a charge current I_c^{app} is injected in the nanomagnet a spin accumulation builds at the interface with the non-magnet, that results in a spin current injection J_z^s. The inverse spin Hall effect in the SOC material converts the spin current into a trasversal charge current I_c^{ISHE}, this charge current will result in a build up of charge that can be measured as a trasversal voltage V_{ISHE} in the open circuit condition.

vertical current density J_z^c is flowing locally through the F/N interface at z=0 it follows from the Valet-Fert model that the spin accumulation can be written as [12]:

$$\mu(z) = \frac{cosh(\frac{h_N+z}{\lambda_N})}{cosh(\frac{h_N}{\lambda_N})}\mu(0) \tag{1.34}$$

in the ISHE material (M) and

$$\mu(z) = \frac{cosh(\frac{h_F-z}{\lambda_F})}{cosh(\frac{h_F}{\lambda_F})}\mu(0) \tag{1.35}$$

in the ferromagnet (F). Where μ, h, λ are the spin accumulation, the thicknesses, and the spin diffusion lenghts, respectively. Assuming a transparent interface, the spin current is conserved so we can write:

$$-\frac{1}{\rho_F^*}\frac{\partial\mu}{\partial z} + p_F J_z^c = -\frac{1}{\rho_N}\frac{\partial\mu}{\partial z} \tag{1.36}$$

where p_F is the polarization of the ferromagnet, ρ is the resistivity of the material and $\rho^* = \frac{\rho}{(1-p_F^2)}$ is the effective resistivity of the ferromagnetic material. By combining equation 1.34 with 1.35 and 1.36 one can obtain the expression of the spin accumulation at the interface:

$$\mu(0) = \frac{p_F J_z^c}{\frac{tanh(\frac{h_N}{\lambda_N})}{\rho_N\lambda_N} + \frac{tanh(\frac{h_F}{\lambda_F})}{\rho_F^*\lambda_N}} \tag{1.37}$$

Locally a transverse charge current density J_y^c is generated through the ISHE effect by the vertical spin current density, according to $\vec{J}_c = \Theta_{SHE}\vec{J}_s \times \vec{s}$ [5] it follows:

$$\vec{J}_c = det\begin{vmatrix} \vec{\imath} & \vec{\jmath} & \vec{k} \\ 0 & 0 & J_z^s \\ 1 & 0 & 0 \end{vmatrix}\Theta_{SHE} \tag{1.38}$$

$$J_y^c = \Theta_{SHE}J_z^s = -\frac{\Theta_{SHE}}{\rho_N}\frac{\partial\mu}{\partial z} \tag{1.39}$$

where Θ_{SHE} is the spin Hall angle. The integration of this current density over the section of the SHE wire gives the transverse current generated by ISHE:

$$\iint_{-h_N}^{0} J_y^c\,dx\,dz = \frac{\Theta_{SHE}}{\rho_N}\int(\mu(0) - \mu(-h_N))\,dx \tag{1.40}$$

Substituting now the expressions for μ found in 1.34 and 1.35, we obtain:

$$I_c^{ISHE} = p_F\Theta_{SHE}\lambda_N\frac{1 - \frac{1}{cosh(\frac{h_N}{\lambda_N})}}{tanh(\frac{h_N}{\lambda_N}) + \frac{\lambda_N\rho_N}{\rho_F^*\lambda_F}tanh(\frac{h_F}{\lambda_F})}\int J_z^c\,dx \tag{1.41}$$

Assuming that the current will distribute homogeneously in the y direction, such that $I_c^{app} = \iint_0^{W_F} J_z^c\,dx\,dy = W_F\int J_z^c\,dx$ hence $\int J_z^c\,dx = I_c^{app}/W_F$ where I_c^{app} is the injected input charge current. The expression for the charge current output in the transverse

heavy metal wire becomes:

$$I_c^{ISHE} = p_F \Theta_{SHE} \lambda_N \frac{1 - \frac{1}{cosh(\frac{h_N}{\lambda_N})}}{tanh(\frac{h_N}{\lambda_N}) + \frac{\lambda_N \rho_N}{\rho_F^* \lambda_F} tanh(\frac{h_F}{\lambda_F})} \frac{I_c^{app}}{W_F} \tag{1.42}$$

In the open circuit condition for the transverse wire we can write the voltage output as $V_{ISHE} = R_T I_c^{ISHE}$, where R_T is the transverse resistance resulting from the parallel between the ferromagnet and the non-magnetic material (see figure 1.9 for reference):

$$R_T = \frac{W_F}{W_N(\frac{h_F}{\rho_F} + \frac{h_N}{\rho_N})} \tag{1.43}$$

so that the spin Hall signal is then given by:

$$R_{ISHE} = \frac{V_{ISHE}}{I_c^{app}} = \frac{p_F \Theta_{SHE} \lambda_N}{W_N(\frac{h_F}{\rho_F} + \frac{h_N}{\rho_N})} \frac{1 - \frac{1}{cosh(\frac{h_N}{\lambda_N})}}{tanh(\frac{h_N}{\lambda_N}) + \frac{\lambda_N \rho_N}{\rho_F^* \lambda_F} tanh(\frac{h_F}{\lambda_F})} \tag{1.44}$$

For systems composed of non-magnetic materials with much shorter spin diffusion lengths than their thicknesses, which is the case for heavy metals $h_N/\lambda_N >> 1$, $h_F/\lambda_F >> 1$, the expression can be simplified as:

$$R_{ISHE} = \frac{V_{ISHE}}{I_c^{app}} = \frac{p_F \Theta_{SHE} \lambda_N}{W_N(\frac{h_F}{\rho_F} + \frac{h_N}{\rho_N})} \frac{1}{1 + \frac{\lambda_N \rho_N}{\rho_F^* \lambda_F}} \tag{1.45}$$

The spin Hall signal R_{SHE} quantifies the rate of the transverse voltage output to the charge current input I_c^{app} and as we can see we get an advantageous dimensional scaling. This signal allows us to read the magnetization state of the nanomagnet. However, the performance of the MESO/FESO logic also relies on the output current. In particular, the produced voltage directly determines the capability of switching the next element in the circuit with the magnetoelectric or ferroelectric effect. The produced current defines the switching energy and delay time. In this framework the normalized current output has to be maximized for the best energy efficiency:

$$\frac{I_c^{ISHE}}{I_c^{app}} = \frac{1}{W_F} \frac{p_F \Theta_{SHE} \lambda_N}{1 + \frac{\lambda_N \rho_N}{\rho_F^* \lambda_F}} \tag{1.46}$$

1.3. The motivation behind this work

The conversion efficiency demonstrated above (see Eq. 1.46), being the current gain of the device, is similar in the case of IREE materials [35] and can be written as:

$$G = \frac{I_{out}}{I_{in}} = \frac{\lambda_{eff}}{W_{FM}} \tag{1.47}$$

where λ_{eff} is an effective length that depends on the specific effect involved in the conversion, and W_{FM} is the width of the ferromagnetic injector. These effects can happen in a large variety of large SOC materials, such as: heavy metals (*e.g.* Pt, Ta, W) $\lambda_{eff} < 1$ nm [5], Bi_2Se_3 $\lambda_{eff} \sim 10$ nm [36], graphene/MoS_2 $\lambda_{eff} \sim 10$ nm [37], $LaAlO_3/SrTiO_3$ $\lambda_{eff} \sim 6$ nm [38] and ferroelectric Rashba semiconductors such as GeTe [7] ($\lambda_{eff} \sim 1$ nm) and SnTe ($\lambda_{eff} \sim 5 - 10$ nm). FERSC give the advantage of a tunable SOC.

In order to make spin-orbit based devices such as the MESO logic, and according to the gain G reported in Eq. 1.47, two strategies are available: (1) the downscaling the FM nanostructure (W_{FM}) and (2) the exploitation of materials with sizeable λ_{eff}. It turns out that such devices are advantageous whenever realized with materials owning λ_{eff} comparable with W_{FM}, the gain can become greater than unit and further increase with the down scaling of the device dimensions.

To reach such goal, I employed the commercial *Nanofrazor Explorer* t-SPL system by *Heidelberg Instruments* (link: Heidelberg NanoFrazor) [39]. Being the *Nanofrazor* still in its infancy, the initial objective of this work was to replicate the devices from Pham *et al.* [10] described in section 1.1.2, in order to optimize and push the Nanofrazor's process to reach the target minimum feature size for spin-orbit based devices.

2 | Methods

This chapter describes the experimental techniques used during my thesis. In the first part, PVD techniques employed for the deposition of materials are presented in section 2.1.1. Then, a detailed description of the distinctive lithographic technique in this work: thermal scanning probe lithography (t-SPL), is given in section 2.2.1. A brief overview of optical lithography can be found in section 2.2.2.

2.1. Thin Film Deposition

In this section some state of the art thin film deposition techniques employed for this work will be discussed. Firstly an overview of the main physical vapour deposition configurations is given, namely: e-beam (2.1.1), thermal evaporation (2.1.1) and magnetron sputtering (2.1.1).

2.1.1. Physical Vapour Deposition

Physical Vapour Deposition (PVD) is a standard technique employed in the growth of thin films. In PVD, particles such as single atoms or molecules travel from a source in high vacuum and reach the surface of the substrate in "line of sight", which is usually fixed upside down on the top of the vacuum chamber, where they condense. PVD divides into to main categories: thermal evaporation and sputtering. In thermal evaporation, the particles are evaporated from a solid or liquid source by using a e-beam or simple Joule effect. In sputtering deposition the source particles are ejected from a solid target bombarded with energetic ions from a cold plasma. The depositions have to be carried out in high vacuum to guarantee the necessary particle mean free path and high purity films. In general, the free surface vaporization rate depends on the temperature and on the vapour pressure of the material which are strongly related. The vapour pressure has an exponential dependence on temperature and, Fig. 2.1 shows this function for several metals commonly evaporated. From the Langmuir-Knudsen theory, the evaporation rate

in g/sec is estimated to be:

$$R_{evap} = 5.83 \times 10^{-2} A_s \sqrt{\frac{m}{T}} P_e \tag{2.1}$$

where A_s is the area of the source, P_e is the equilibrium vapour pressure of the material at the evaporation temperature in $torr$, m is the molecular mass in grams. A good deposition rate is achieved with at least 10^{-2} Torr vapour pressure, one can control the evaporation power and therefore the temperature of the source to adjust this parameter [40].

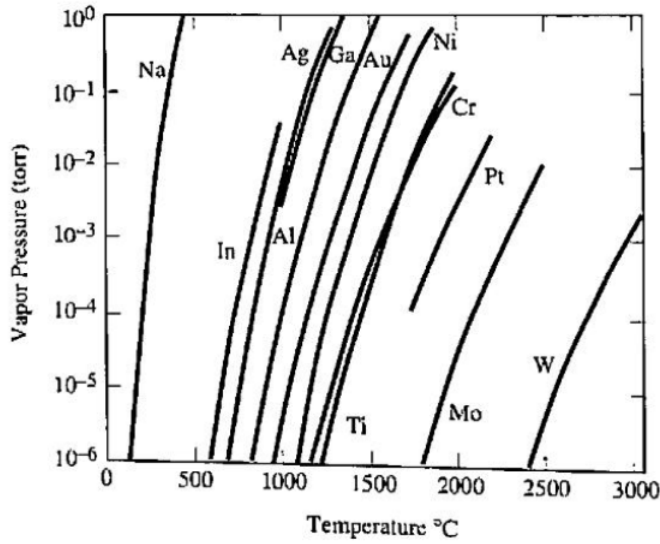

Figure 2.1: Vapour pressure as a function of temperature of commonly evaporated elements.

The deposition rate is controlled by standard quartz microbalances located in the chamber. The evaporation rate is a function of source and chamber geometry. For simplicity we can firstly approximate the source as a point and then consider a more realistic case of a small area source. For uniform and isotropic emission, which can be expected from an ideal thermal Maxwellian distribution of velocities, the source has circular symmetry in two dimensions or spherical in three dimensions. For a point source one can derive an expression for the deposition rate ν of a film deposited on a flat surface as a function of the distance between source and substrate. The expression of the incoming flux normal to the sample surface in a particular spot k can be written as [41]:

$$F_k = \frac{R_{evap}}{\Omega r^2} \cos \theta_k \tag{2.2}$$

where R_{evap} is the evaporation rate from the source, r is the distance from the source, Ω

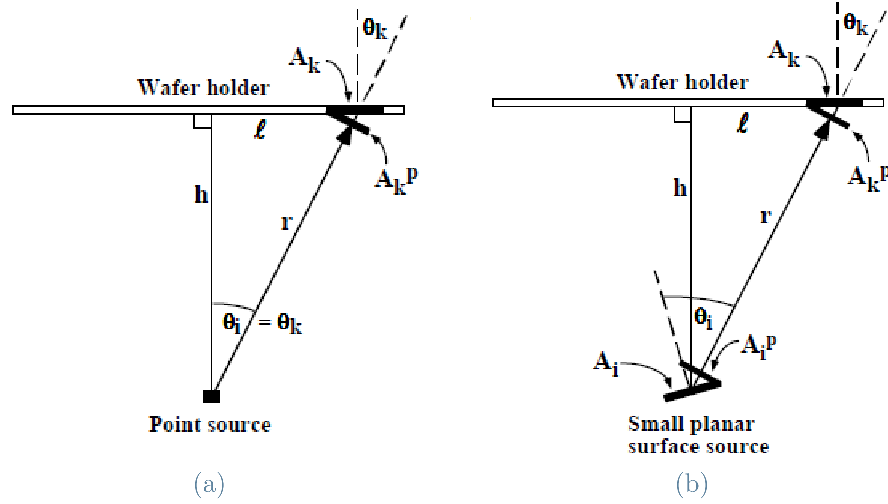

Figure 2.2: **(a)** The geometry and coordinate system used in modelling point source PVD systems. Here, a portion of the substrate surface A_k sits on the wafer holder at an angle θ_k with respect to the holder's normal and it's coated by the incoming material flux from an isotropic emitting point source. **(b)** A more realistic situation with a small planar source. In this case, the projected area of the source A_i^p as seen from the spot A_k on the substrate is taken into account. Adapted from [41].

is the emission solid angle (2π for an upward emitting point source) and θ_k is the angle between surface normal and the direction of the source to a spot on the surface (see Fig. 2.2 for reference). This flux corresponds to the amount of material deposited per time per unit surface area. The deposition rate ν in $Å/s$ on an area A_k in m^2 is the flux F_k in g/s divided by the density of the material which is being deposited ρ in g/m^3, so that:

$$\nu = \frac{R_{evap}}{\Omega \rho r^2 10^{-10}} \cos\theta_k \tag{2.3}$$

A more realistic approximation is to consider a small surface area source.This kind of source, similar to what happens in Knudsen cells as well, displays the so called cosine distribution law or ideal cosine distribution. The emitted flux distribution is not uniform in all directions as with an ideal point source but is more directed and dependent on the projected area of the small source area towards the flux direction. While it may not be intuitively obvious that this Knudsen-cell like behavior should apply to evaporation from a small surface, it has been verified experimentally by Knudsen himself [42] and others for many materials. This cosine behavior is also recurring in other problems in physics such

as black body radiation and perfectly diffusing surfaces in optics. Equation 2.3 becomes:

$$\nu = \frac{R_{evap}}{\pi \rho r^2} \cos\theta_k \cos{\theta_i}^n \tag{2.4}$$

Where θ_i is the angle between the source and target surfaces normals (see Fig. 2.2 for reference). The n factor takes into account deviations from the ideal cosine law, a larger n means a more directional emission. To achieve the best possible film uniformity with these kind of sources, rotating hemispherical wafer holders are employed. Thermal evaporation is a reliable deposition method which offers high film purity and absence of any damage to the substrate but it also has some limitations. Alloys and compounds are difficult to evaporate with thermal PVD techniques due to differences in the vapour pressures of the species. Line of sight evaporation and high sticking coefficients in isotropic evaporation lead to poor step coverage because of the limited range of arrival angles and absence of particle diffusion after condensation.

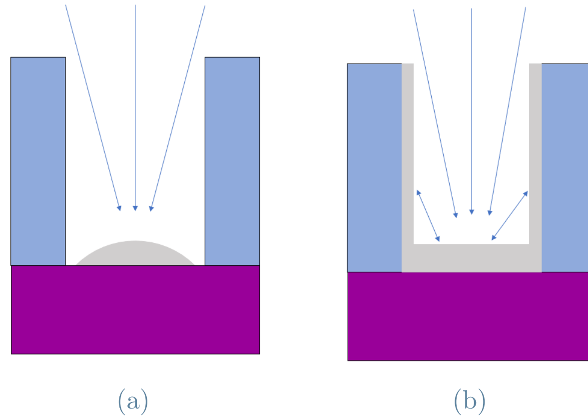

Figure 2.3: **(a)** is shown a situation where the sticking coefficient is close to 1 so the species are deposited where they first strike. **(b)** the sticking coefficient is much less then one which means that there's more diffusion and remission that leads to a more conformal film.

E-beam Evaporator

E-beam deposition tools are among the most common PVD tools for industrial or research applications. An electron beam is generated by thermoionic emission in a tungsten filament. These electrons are accelerated away from the filament with a positive biased electrode (the anode) to energies in the order of keV. The electron beam is guided toward the material to evaporate by a proper magnetic field. The energy release by electrons to

the material provokes its melting or sublimation and permits to achieve a suitable vapour pressure for deposition. The crucible is made of materials capable to resist high temperatures (BN, Alumina, tungsten, graphite, etc.). A water-cooled shroud minimize the contamination possibly coming from the side-walls of the crucible. The e-beam heating system is able to provide enough heat to evaporate very high melting temperature heavy metals, e.g. Pt and Ta, with rates in the order of $1Å/s$. A schematic representation of an e-beam evaporator and its operation is shown in Fig. 2.4a.

An *Evatec Bak 640* is available at Polifab (see Fig. 2.4b) which allows multilayer deposition from a six pocket rotating crucible. The chamber is pumped by a cryogenic pump which guarantees processes in high vacuum, with pressures in the order of $10^{-6}mBar$.

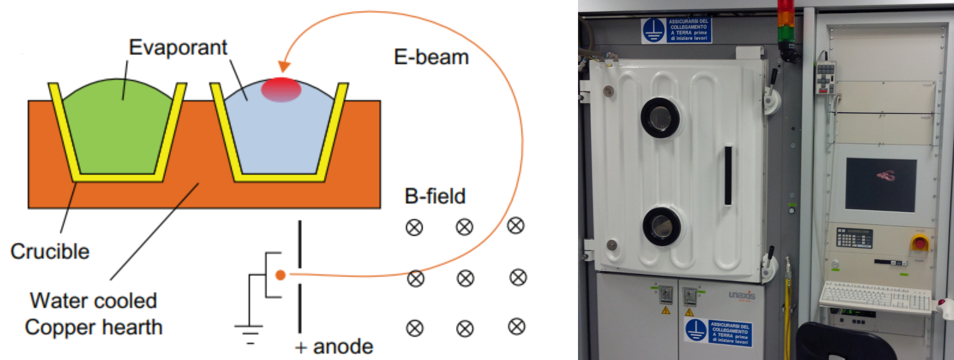

Figure 2.4: **(a)** Sketch of an e-beam evaporator. **(b)** Photograph of the *Evatec Bak 640* e-beam evaporator. A base pressure of $10^{-6}mBar$ is obtained by using cryogenic pump. It allows the deposition of multilayers using six crucibles, with an on-flight control of deposition rate and thickness through quartz microbalances.

Thermal Evaporator

Whereas the e-beam evaporator melts the source material locally, in thermal evaporator the whole crucible is heated. This limits the range of applicability of this tool. An high electric current flows through heating tracks, called "boats", that melt the desired evaporation material, due to the Joule effect. Powers in the order of hundreds of watts are required for rates in the order of $1-2Å/s$. This kind of heating is easier and cheaper to realize with respect to e-beam evaporation but the high power required to completely melt the source material for the evaporation introduced huge limitation on the range of materials suitable for TE. Oxydes and some metals with high melting point cannot be evaporated this way. As film uniformity, step coverage and evaporation profiles, this technique is analogous to other thermal systems.

The thermal evaporator present at Polifab is the *Moorfield Minilab 080* (see Fig.2.5). The high vacuum environment is obtained by a combination of rotary and turbo molecular pumps to a pressure in the order of $10^{-6} mBar$.

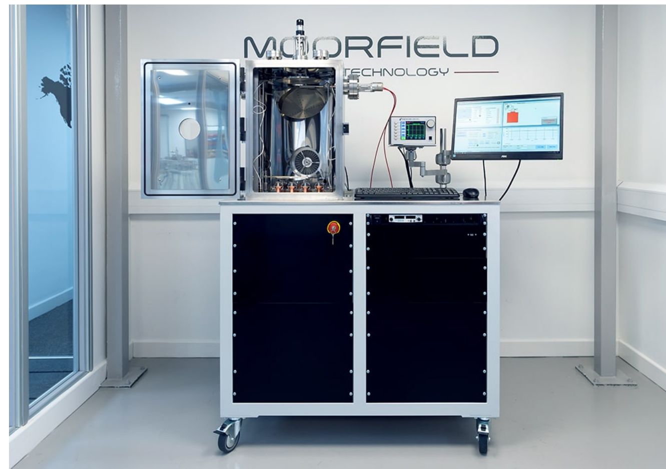

Figure 2.5: The *Moorfield Minilab 080* is a compact standardized configuration for a thermal evaporation system that allows for multilayer deposition with fully automated process control.

Magnetron Sputtering Deposition

Magnetron sputtering is another deposition technique, which allows good film adhesion to the substrate, better step coverage than thermal PVD systems and high control on the thickness, uniformity and composition of the deposited material [41]. Compounds and alloys can be easily deposited with this technique as the vapour pressure of the single species doesn't matter anymore. By first creating a cold plasma in which the mean velocity of the positive ions is directed into some source material, the source material surface is eroded by the arriving ions via energy and momentum transfer; either individual atoms, clusters of atoms or molecules are ejected in the form of neutral particles. As these neutral particles are ejected, they will travel in a straight line unless they come into contact with something – other particles or a nearby surface. If a substrate is placed in the path of these ejected particles, it will be coated by a thin film of the source material. The cold plasma, which is ignited through a DC bias for conductive targets or a radio-frequency (RF) field for insulators, contains neutral inert gas atoms (commonly Argon) and roughly an equal number of positive ions and free electrons. The free electrons from the Ar+ ions are immediately accelerated by the field and ionize by collision even more Ar atoms. This cascade process ignites the plasma. At this point, the Ar+ ions are accelerated towards a biased electrode, striking the surface and releasing source material and more free electrons

by energy transfer. Fig. 2.6 summarizes the processes characterizing a cold plasma.

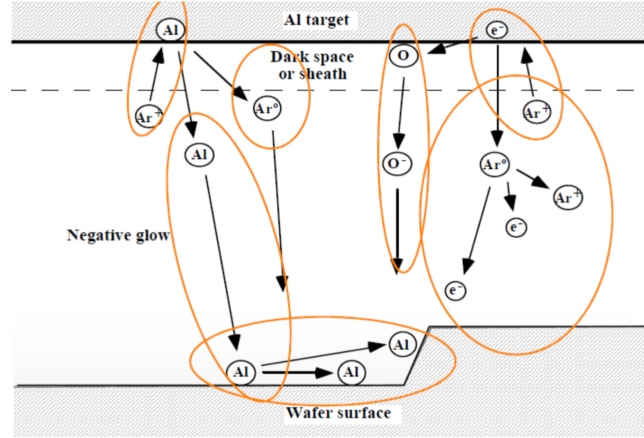

Figure 2.6: Processes characterizing the cold plasma during sputtering. Accelerated Ar ion sputters a target atom (*e.g.* Al). The Al migrates to the wafer surface where it can: stay absorbed, diffuse to another surface site or be re-emitted. The Ar ion can be neutralized during sputtering and incorporated in the growing film, secondary electrons can be emitted by the target during sputter and they can: ionize an impurity that travels to the wafer surface or ionize Ar and sustain the plasma.

The emission profiles in sputtering deposition allows to achieve a wide distribution of arrival angles, which generally improves step coverage. Fig. 2.7 shows a representation of this concept. But there are other factors that improve step coverage in sputtering systems. Because of the high pressure in these systems, the atoms experience more gas phase collisions with particles in the plasma. One can estimate the average number of collisions by calculating the mean free path, λ, of a particle in a gas. From kinetic theory, the mean free path of a gas particle is [43]:

$$\lambda = \frac{k_B T}{\sqrt{2}\pi d^2 P} \tag{2.5}$$

where k_B is the Boltzmann constant, T is temperature, d is the collision diameter of the molecule or atoms (about $0.4nm$ for most particles of interest). In a typical sputtering system with $P = 5$ mtorr, which is exactly the pressure at which the Pt was sputtered in this work, this results in a mean free path of the order of 1 cm, which is less than the physical path length the depositing atoms follow. The collisions result in a more isotropic flux.

Magnetron sputtering exploits permanent magnets located behind the target to achieve two advantages: first, the free electrons in the plasma are prevented from bombarding

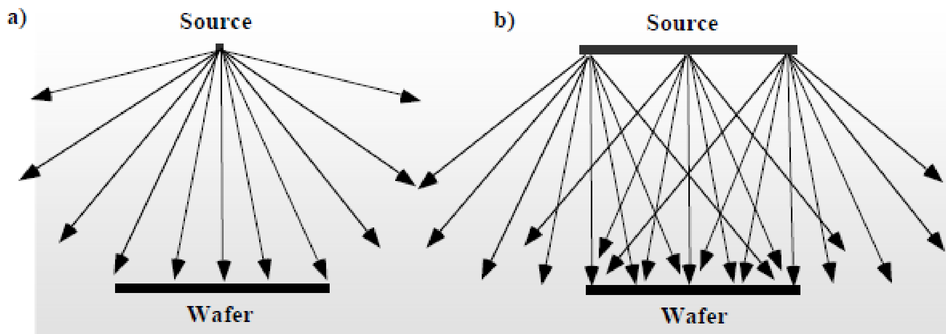

Figure 2.7: **(a)** Arrival angles distribution from a small or point like source as modelled in thermal systems. **(b)** Sputtering targets provide a wide range of arrival angles. Adapted from [41].

the substrate, which would cause overheating and structural damage; second, the circular paths carved by the free electrons along the lines of the magnetic field enhance the probability of ionizing neutral Ar atoms. The higher number of available ions significantly increases the rate of erosion of the target and allowing for a reduce pressure at the same deposition rate.

Fig. 2.8a shows a sketch of a typical sputtering deposition tool. At Polifab, the *AJA ATC Orion 8* (see Fig. 2.8b) magnetron sputtering system offers a thickness uniformity of about ±2% over 3" wafers. It's best suited to easily deposit heavy metals such as Pt or Ta, alloys such as CoFeB or oxide compounds. The main deposition chamber is cryo pumped to a base pressure in the order of 10^{-9} torr.

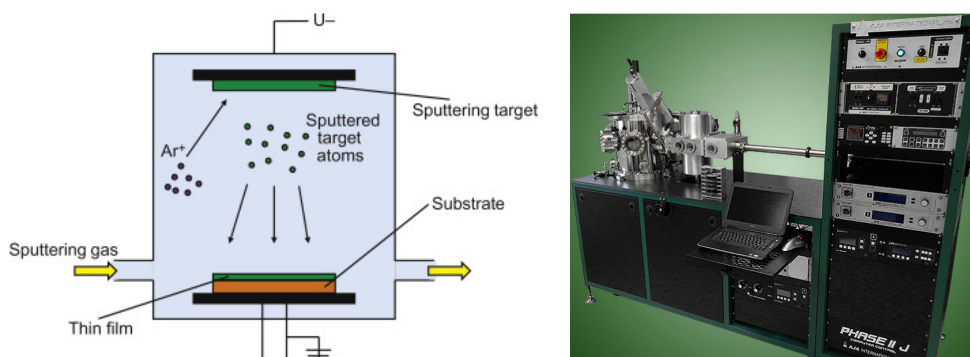

Figure 2.8: **(a)** Sputtering tool sketch. Inside the vacuum chamber, a cold plasma of Argon is generated with an RF or DC field. The Argon ions in the plasma are accelerated to the target and they knock out atoms with their kinetic energy and momentum. **(b)** The *AJA ATC Orion 8* sputtering system is an integrated deposition tool which features DC or RF plasma operation, enabling sputtering of conductive or insulating materials.

2.2. Lithography

In this section a general overview of the lithographic techniques employed for this work will be given. The smaller features of the spin-to-charge conversion devices were patterned at the nm scale to maximize the electrical signal, which increases as the lateral dimension shrinks [10]. The following paragraphs will first introduce a new state of the art lithographic technique called thermal scanning probe lithography which was employed in this work to achieve nm resolutions. After that, some information on traditional optical lithography is given.

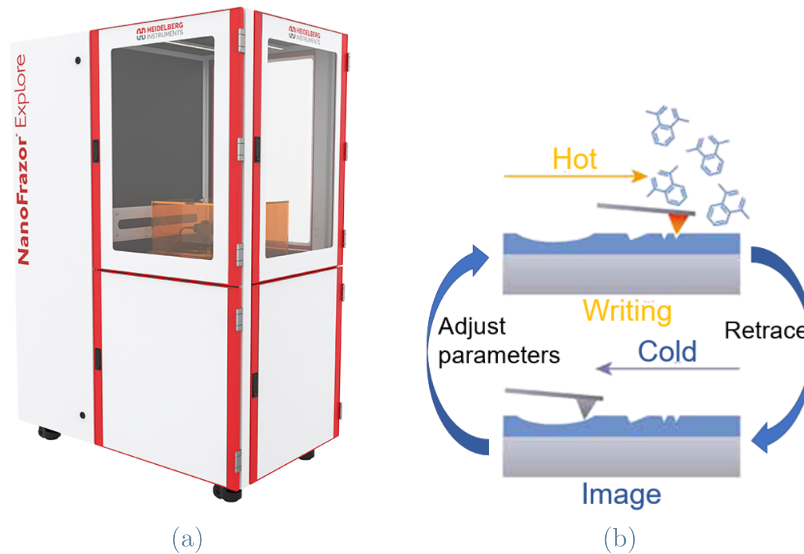

(a) (b)

Figure 2.9: **(a)** The *Heidelberg NanoFrazor Explore* is the first commercial t-SPL tool, with an hybrid direct laser sublimation and greyscale patterning capability in a single fabrication step. In-situ imaging enables two unique features: markerless overlay, and comparison of the written and target patterns during writing, so the parameters can be immediately adjusted. **(b)** A representative sketch of the NanoFrazor closed loop lithography concept which enables extreme vertical (indentation depth) and lateral resolution.

2.2.1. Thermal Scanning Probe Lithography

The Polifab cleanroom hosts the first commercial thermal scanning probe (t-SPL) tool: the *NanoFrazor Explore* from *Heidelberg Instruments*(see Fig. 2.9). At the core of this innovative method of doing lithography there is an ultra-sharp heatable probe tip which is used for writing and simultaneous inspection of complex nanostructures. The heated tip creates arbitrary, high-resolution nanostructures by local sublimation of thermal resists

such as Polyphthalamide (PPA). In addition to its capabilities in processes that involve resist sublimation, t-SPL is also very interesting in other sort of applications, namely: local physical/chemical material conversion or addition. Most of today's t-SPL tools, like NanoFrazor, control the tip temperature via a resistively heated element incorporated into the cantilever above the tip. Owing to the small size of the heating element (few micrometers) and the cantilever (tens of micrometers) with nanometric tips, the cantilever's thermal constant is on the order of a few microseconds, which produces ultra-fast heating and cooling. The system offers ultra-high resolution (<10 nm half-pitch demonstrated in resist [39]) with no artifact corrections required and without being limited by diffraction. A brief overview of the possible t-SPL fields of application can be found in Fig. 2.10. For this work, t-SPL is exploited in the so called "bilayer lift-off" process, which will be described in detail in chapter three.

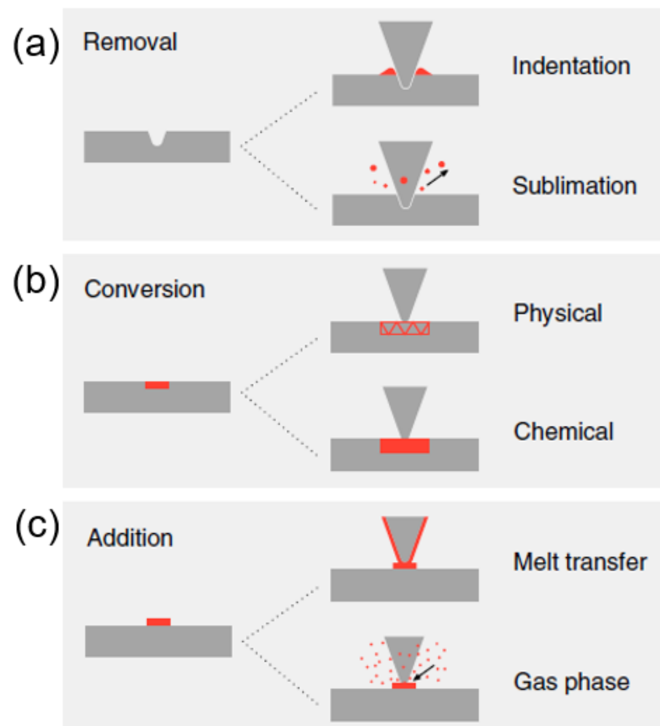

Figure 2.10: Overview of concepts of local modifications induced by a t-SPL on a sample. **(a)** Removal of material by thermomechanical indentation or sublimation of a sample material; **(b)** conversion of a sample by local modification of its physical properties such as the crystallinity or magnetic/ferroelectric dipole orientation, or chemical conversion; **(c)** addition of a functional material by melt transfer from a heated tip to the substrate or from a gas phase such as chemical vapor deposition of a precursor material. Adapted from [44].

Figures of merit

t-SPL offers the following advantages [44].

Heat exchange. *Heat* is an universal stimulus that can induce functional modifications to a wide range of materials without strict physical boundaries on the limit resolution. In contrast to other techniques that present fundamental limits on the achievable feature size, such as the diffraction limit in optical lithography or the scattering of electrons in the resist in electron beam lithography (EBL).

Absence of charged particle bombardment. Contrary to EBL, no charged particles are present: t-SPL induces material modifications via phonons instead of exposure to charged particles such as electrons or ions, thereby avoiding unwanted creation or scission of covalent bonds, lattice defects, vacancies or trapped charges, which are especially a concern when working with atomically-thin 2D materials. In contrast, t-SPL can readily produce residual- and damage-free surfaces that lead to dramatic enhancements in device performance, and without requiring complicated contact engineering or instrumental setups. An example of this capability was demonstrated in a work published in *Nature Electronics* [45], in which metal contacts with vanishing Schottky barrier were fabricated with t-SPL on MoS_2 monolayers.

Absence of proximity effect. The scattering of electrons in EBL leads to the so called proximity effects. The proximity effect in EBL is the phenomenon in which the exposure dose distribution, and hence the developed pattern, is wider than the scanned pattern, due to the interactions of the primary beam electrons with the resist and substrate. These cause the resist outside the scanned pattern to receive a non-zero dose which is an artifact that can be difficult to correct at high resolutions.

Ultra-sharp tip. A heated tip with an apex diameter below 10 nm can produce complex geometries with a lateral resolution below 10 nm [39], which is more than one order of magnitude better than direct-write laser lithography and comparable to the best possible resolution achievable with state of the art EBL tools. The fact that t-SPL is a novel technique still in its infancy stage should be taken into account in the comparison with the well established EBL.

Feedback-loop lithography. Today's t-SPL tools precisely control the actuation force and the tip-sample contact duration, thereby enabling 3D indentation with vertical resolution better than 1 nm [46]. This feature is called grayscale patterning which means that the topography can include a vertical degree of freedom.

Ambient pressure operation. The components of a t-SPL tool are relatively simple

and cost-effective compared to focused electron or ion beam systems. The whole system is compatible with ambient environments which means that an high vacuum chamber is not necessary.

***In-situ* imaging**. In addition to patterning, the t-SPL tip can image the surface topography before, after and during patterning, similarly to an AFM tip (with the tip heating turned off). To maintain a high t-SPL patterning quality during writing, software algorithms compare the actual and the target topography in real-time and adapt patterning parameters such as the actuation force.

Marker-less overlay. The alignment of new structures above the existing ones (overlay) is a crucial step in every step of the process. In traditional lithography techniques markers are added in the layout in order to align previously patterned structures with new ones. However, alignment in the nanometer regime is not a trivial task even with markers. The *in-situ* inspection capability of t-SPL enables precise overlay and marker-less stitching as samples can be imaged before patterning to locate previously patterned structures or flakes of 2D materials.

Challenges

The following challenges currently limit the application range of t-SPL [44].

Throughput. The throughput is limited by the mechanics which can provide scan speeds for a single tip of a few nm/s [47].This speed is comparable to that of EBL or ion beam lithography operating at their highest possible resolution. Using multiple tips in parallel ultimately could overcome the throughput limit for t-SPL [48]. Another strategy to increase throughput for applications that involve both microscale and nanoscale structures is to combine a high-resolution t-SP with a fast integrated laser writer in a single tool. For this reason, the NanoFrazor Explore offers a 405 nm laser in addition to its thermal tip. The throughput of this laser is higher because a much larger distance is covered during scanning for each pixel with respect to the tip.

Tip consumption. The tip will suffer an unavoidable irreversible deterioration due to friction and contamination. The attainable resolution reduces with tip use, regular exchange of the cantilever is required.

Contact temperature. The small tip-sample contact area makes it difficult to precisely determine the contact temperature. This restriction is less of an issue for applications that do not require high temperature or precise knowledge of the tip-sample contact temperature, because the optimal patterning parameters can be directly determined from

the sample response using the in situ AFM capability of the t-SPL tools.

Performance Parameters

In t-SPL, the tip contact *temperature* is the key parameter governing material modifications and determines the attainable resolution and patterning speed. If the temperature is too low there may be incomplete or absence of material modifications, whereas when the temperature is too high resolution might be lower due to heat diffusion [44]. In the next section a simplified heat transfer model is proposed, while in the following list some qualitative considerations on this topic are enumerated.

Tip-apex diameter. The most important factor to achieve the best possible resolution is of course the tip apex diameter. There is however a limit given by boundary phonons scattering: once the tip diameter is smaller than the mean free path of phonons (in silicon $\sim$ 70–140 nm) the heat transfer through the tip is strongly reduced [49].

Thermal conductivity. The substrate thermal conductivity influences the tip-sample contact temperature. An higher thermal conductivity means lower contact temperature, as heat is transported away from the source more efficiently. For thin films on a bulk substrate, the influence of the substrate thermal conductivity on the tip-sample contact temperature depends on the film thickness. For a film thickness ten times larger than the tip apex diameter, the influence of the substrate thermal conductivity can be neglected [50]. For this reason, a thick resist layer ($> 50nm$) can be employed to avoid any influence from the substrate or to protect temperature sensitive materials below.

Activation energy. The activation energy defined as the potential barrier for the heated atoms or molecules to overcome, determines the temperature sensitivity of the reaction rate and how much material is converted or sublimated at a specific temperature.

Tip-sample contact duration. The contact duration directly affects the kinetics of a reaction. It is important to note that the tip-sample contact duration necessary to induce a material modification can be as short as a few microseconds.

Tip-sample contact force. The contact force affects the temperature and, potentially, the reaction kinetics of the t-SPL process. A higher force on the cantilever increases the effective tip-sample contact area for more efficient heat transfer and the contact force exerts a local pressure in the material under the tip, which can affect the reaction kinetics itself by reducing the reaction activation energy.

Heat Transfer Model

The performance of a t-SPL cantilever depends on the temperature distribution within the cantilever and cantilever tip. In the case of resistive heating near the tip, the heat flows either to the substrate or through the cantilever and then to the substrate. Heat flows through the cantilever by conduction, and from the cantilever to the environment by conduction and thermal radiation. The thermal conductance of a silicon heated cantilever is about 1 $\mu W/K$ when it is operated to heat a substrate as shown in Fig. 2.11, together with the thermal resistance model. About 30 % of the total heat generated flows from the heater, across the air gap, and into the substrate [51]. The rest of the heat flows down the cantilever legs and eventually nearly all of this heat flows into the substrate. Usually, convection and radiation are negligibly small. From the values of the thermal resistances one can see that the quantity of heat transferred through the tip is much smaller than that through the air gap. However, the heat flux at the tip-sample contact is large, such that the interface temperature at the contact is much higher than the temperature rise by air conduction. For most substrates, heat conduction across the cantilever-substrate air gap has a small effect on the tip-sample interface temperature [49]. Theoretical treatments of thermal contact conductance through a nanometer-scale constriction provide insights into heat flow through a t-SPL cantilever. Typical thermal contact conductance is in the range 0.1–100 nW/K [49], taking both experimental data and simulation. In humid air, a water meniscus forms at the tip-sample contact [52]. For a wetting surface and relative humidity of 50 %, the liquid contact diameter is about 30 nm, somewhat larger than a typical solid contact diameter of about 10 nm [50]. The liquid film conductance is very low so significantly more heat flows through the solid than the liquid and the resolution is not affected.

Cantilever Technology

The first implementation of t-SPL used a laser to heat the cantilever. The integration of an heating laser in an AFM system can be challenging, but nearly any cantilever can be heated this way. Resistive heating is the method of choice for modern t-SPL tools. Metal wires or metal junctions can be used for resistive heating, with the junction which can also serve as a thermocouple. The best performance nowadays is given by silicon tips with integrated resistive heating, which can reach temperatures over 1000 °C and have a thermal constant as fast as 10 μs. These cantilevers also have a large temperature coefficient of resistance (TCR) compared to metals, allowing sensitive temperature measurement.

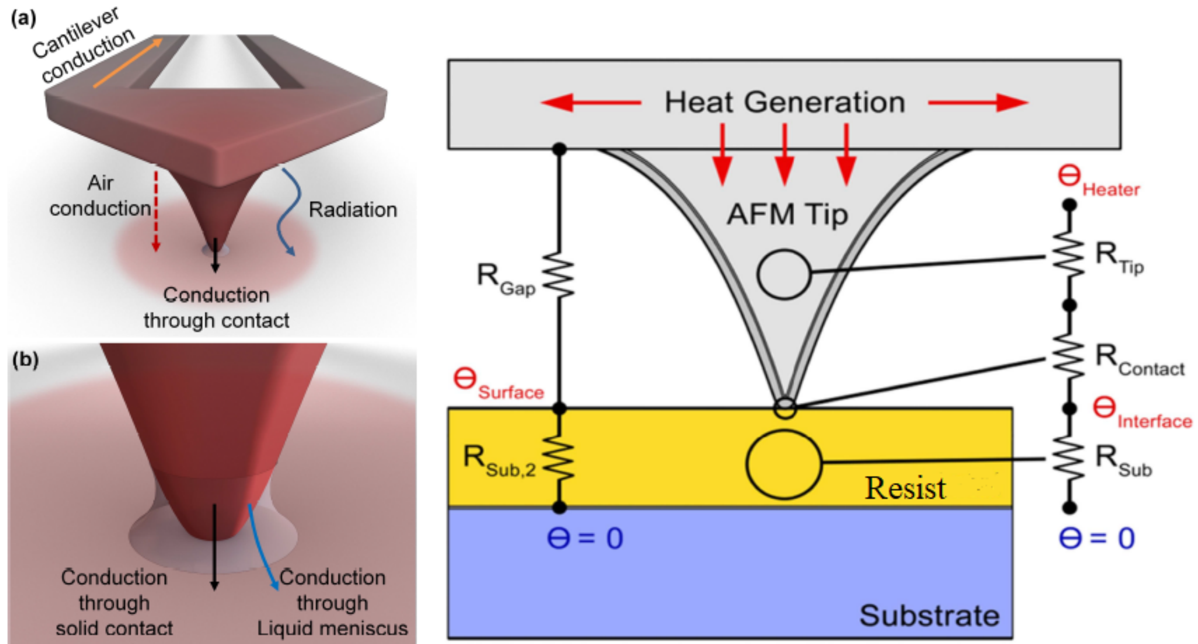

Figure 2.11: The figure shows the heat transfer from a heated cantilever and cantilever tip. Heat transfer from the heaters is mainly due to conduction within the cantilever and cantilever tip, and through the air near the cantilever. Heat transfer at the tip-substrate contact is mainly due to solid-solid contact, although the presence of water at the tip-substrate interface can also affect the heat transfer. Adapted from [49].

2.2.2. Optical Lithography

Optical lithography is of paramount importance in modern Integrated Circuit (IC) fabrication. Virtually all ICs manufacturers today rely on this technique to imprint pattern with sub-micron resolution on a given substrate. In this kind of lithography a light sensitive resist is selectively exposed by shining light through a mask or by sequentially scanning the surface with a laser beam. The resist layer is applied on the surface via spin coating. The incident light intensity multiplied by the exposure time gives the incident energy in J/cm^2, also called dose D, across the surface of the resist film [53]. There exist two main types of photoresist: positive and negative photoresist. In *positive photoresists* radiation induces a chemical reaction in the exposed areas, altering its solubility, while the non-irradiated areas preserve the solubility of the resist itself as shown in Fig. 2.12 on the left. Since UV radiation is attenuated passing through the resist, the deeper the analyzed area, the less the photoresist is activated: this means that at the top of the film there is a higher degradation, while a minor one is expected for bottom layers, and this overcut reflects in profiles of the photoresist as shown in Fig. 2.13a, typically with angles on the order of 75 ° - 85 °. While, in the above mentioned case, the energy provided by

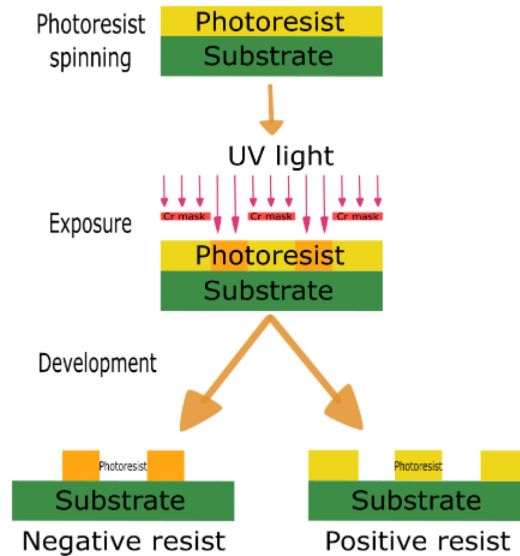

Figure 2.12: Representation of the optical lithographic methods for positive and negative resists. For positive resist the exposed areas are removed during development, whereas in the other case the negative image of the mask remains.

the light source is used to break the chemical bonds of the polymer, in *negative photoresists*, the exposed zones experience a cross-linking effect *(i.e.* polymerization). Here, the irradiated areas are made insoluble: it follows that this insoluble layer forms a "negative" pattern as shown in Fig. 2.12 on the right. Besides these two main classes of photoresists, it exists another special type of photoresist which permits to obtain either positive or negative behaviour, such that more pronounced undercut resist sidewalls and optimized lift-off processes can be achieved (see later for "lift off"): this is the so called image reversal photoresist. This undercut concept is shown in Fig. 2.13b.

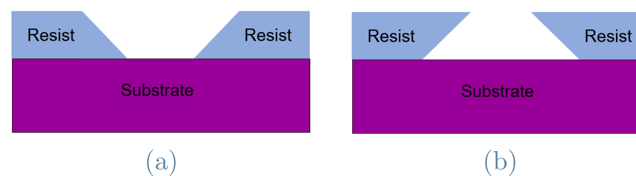

Figure 2.13: In **(a)** the resist "overcut" due to attenuation of the light during its propagation in the resist is shown. The angles are close to 90° in reality. In **(b)** the resist "undercut" is shown, this profile allows for optimized lift-off and can be achieved by inverting the photoresist.

The last and most critical step in optical lithography is the resist development which transforms a latent image into a real relief image. To develop this latent image, the

sample is immersed in a chemical solution that depends on the resist which is being used. For positive photoresist, exposed areas will be removed, while for negative one, the unexposed ones. The imprinted pattern is then used as a mask for other additive or subtractive fabrication techniques such as metal deposition or sputtering.

The industrial standard of exposure tools today is the 193 nm UV optical lithography with physical masks, called "step and scan". The main optical tools employed for this work at Polifab were the 365 nm *Heidelberg Maskless Aligner* (MLA) and the 405 nm laser integrated in the *NanoFrazor*, which are both direct sequential writing lasers. These tools give the advantage of flexibility and faster prototyping thanks to the absence of a physical mask. The *NanoFrazor*'s laser directly patterns on the same thermal resist used for t-SPL and allows for faster writing. However, the speed is lower compared with MLA and the maximum feature size is limited to more then 2 μm (PPA is not a designed for optical lithography). Thus, the core of the devices was realized by t-SPL, then some optically feasible features are patterned *in-situ* on PPA and finally the MLA is employed to finalize the electrical contacts to interface with measurement instrumentation.

3 | Fabrication

In this chapter, every step of the process aimed at obtaining scaled spin-to-charge conversion devices will be explained in detail. While the general aim of the thesis is to obtain a resolution around 50 nm with t-SPL and a resist-based approach, the purpose of the specific device is to exploit spin-to-charge current conversion to process the magnetization state (read-out or processing capability of MESO-like logic). Those devices consist of a heavy metal nanostructure which comprises a main channel grounded on one side (black coloured in Fig.3.1), contacted with transversal Hall-bars for signal readout (A-B in Fig. 3.1) and longitudinal resistance measurements (D-G or C-E in Fig. 3.1). The longitudinal resistance measurements are useful in estimating the resistivity/quality of the heavy metal, as well as in the quantification of the spin-to-charge conversion process (see Eq. 1.46). A nanomagnet (coloured in red in Fig. 3.1) is patterned on top of the heavy metal and used for the injection of spin polarized currents in the channel. The electrical signal generated via inverse spin-Hall effect is then sensed by conventional output contacts with an ammeter (I_{ISHE}) or equivalently with a voltmeter (V_{ISHE}) in the open circuit condition. In order to practically realize such device, I designed a lithographic process consisting of three steps, one for each part of the device:

1. a first step for the heavy metal structure;
2. a second for the ferromagnetic layer;
3. a last step to realize electrical pads suitable for wire bonding.

The NanoFrazor, which is the distinctive lithographic tool, will be employed in the so called "bilayer lift-off" process within the first and second step. Firstly, a structure with nanometric features is be patterned with the NanoFrazor and, after development, the heavy material (Pt or Ta) is deposited with either e-beam evaporation or magnetron sputtering. In the second step, the pillar of ferromagnetic injector (made of either CoFeB or NiFe) is aligned and deposited on top of the previous layer; note that the the *in-situ* reading capability of the NanoFrazor is essential for this overlay. Once the core of the device is created, another step is performed to make output electrical contacts large enough to allow bonding or measurement probes landings and this is done by conventional

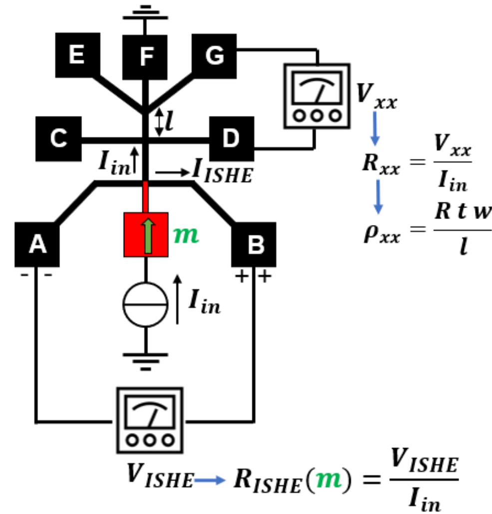

Figure 3.1: Complete device sketch with the heavy metal (in black) and the nanomagnet (in red). A current I_{in} is injected in the magnet which has a magnetization m in plane. The spin accumulation at the interface with the heavy metal leads to a spin-current injection (out of plane). The spin-current is converted in a trasversal charge current I_{ISHE} which leads to a charge accumulation that can be measured as a voltage V_{ISHE} in the open circuit condition. Additional transversal electrodes are contacted to measure the longitudinal resistivity of the heavy metal.

optical lithography (MLA). More information on the "bilayer lift-off process" is given in the following paragraphs and a schematic picture can be found in Fig. 3.9.

3.1. The art of the Nanofrazor

In this paragraph the practical operation of the first commercial t-SPL tool will be deepened. At first, some details on the calibration of the tip will be discussed. Then, the fine tuning of critical parameters for writing and reading (*e.g.* the writer temperature, the height, force pulse duration etc.) will be presented. As probably will become much clear at the end of the chapter, the term "art" indicates that t-SPL, although implemented in a commercial tool, is still rather experimental. A significant effort in optimization is required to achieve nanometric resolution. Of course, mastering the NanoFrazor opens unprecedented possibilities in phase change materials as well as in 2D materials. The following analysis will highlight both the physical working principles and the experimental experience acquired in this work.

3.1.1. Calibrations of the tips

Surface approach/retract calibration

The procedure begins with the tip of the NanoFrazor's thermal cantilever separated from the surface by several micrometers. The NanoFrazor moves the cantilever towards the surface of the substrate by the z-piezo scanner. The z-piezo scanner incorporates a deflection sensor, which is calibrated before being installed in the NanoFrazor. Two properties are exploited in thermoelectric sensing: (1) the heat conduction through the air depends on the convection thermal resistance R_{Gap} (according to the heat transfer model that can be found in section 2.2.1), and (2) the electrical resistance of the Si heater is a strong function of the temperature, which in turn depends on the substrate cooling and thus on the substrate distance [54]. The extension of the piezo scanner reduces the air gap separating the substrate and the cantilever's thermal distance sensor. Consequently, the heat flux increases and the sensor cools down. The resulting variation of the electrical resistance is due to the exponential variation of carrier concentration in semiconductors with temperature: when the sensors cools down the resistance increases and the measured voltage increases if the current is fixed. Fig. 3.2 shows a graph of the data collected during this procedure. Once the tip touches the surface, the reader-to-surface distance

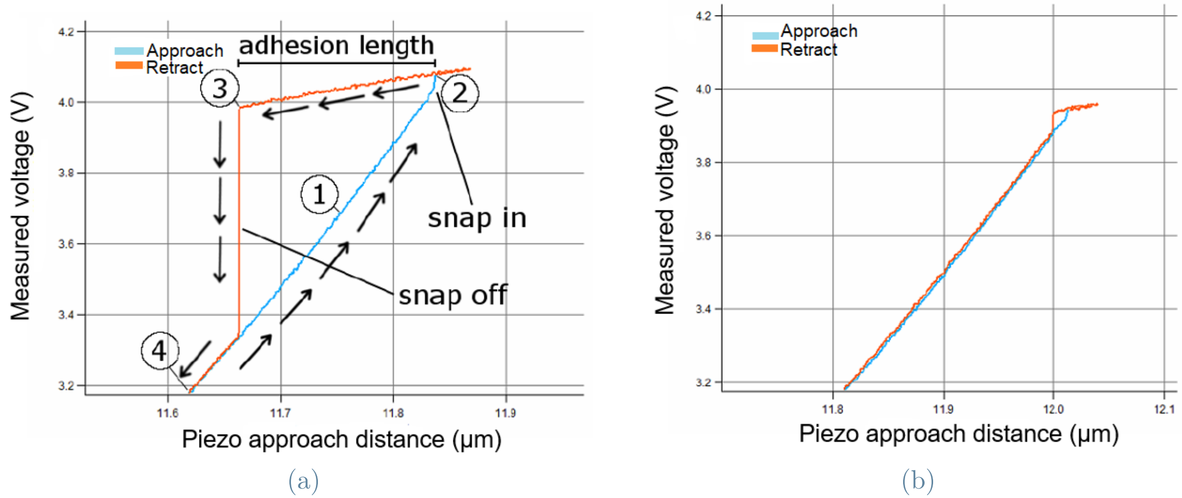

Figure 3.2: **(a)** Approach/retract curve; at point 1 the cantilever is moving towards the surface and so the reader voltage increases. Point 2 shows the so-called "snap-in" event. At point 3, the elastic restoring force of the cantilever is bigger than the adhesion force between the tip and the surface, and the tip "snaps-off". The difference in piezo extension between point 2 and point 3 is called the "adhesion length". At point 4 the cantilever's separation from the surface is controlled only by the z-piezo's position. **(b)** A pristine sharp tip with a short adhesion length (below 50 nm).

is determined by the length of the tip, and the reader signal stops increasing. This is

the so-called “snap-in” event where short range, attractive adhesion forces pull the tip in contact with the surface. The change in slope signals to the NanoFrazor that the surface has been found and it begins to withdraw the cantilever from the surface while continuing to record the reader signal. Initially, during retraction, the tip is kept in contact with the surface by adhesion forces. At some point, the elastic restoring force of the cantilever is bigger than the adhesion force between the tip and the surface, and the tip “snaps-off”. The withdrawal continues until the cantilever returns to its original height above the surface. The difference in piezo extension between the snap-in and snap-out points is called the “adhesion length”. One can estimate the diameter of the tip from the adhesion length calculated from the approach and retract graph. A tip in good condition has an adhesion length of 10 to 50 nm and this roughly corresponds to the diameter of the tip, because the adhesion force between the surface and the tip depends on the contact area. Note that the exact ratio between adhesion length and diameter of the tip depends on the microscopic properties of the substrate surface, on the relative humidity, on the exact shape of the tip and the stiffness of the cantilever. Friction and contamination wear the tip out and it becomes blunt, the adhesion length increases and the performance gets worse (wider indentations).

Temperature calibration

The NanoFrazor’s cantilever contains integrated resistive micro-heaters for patterning (“the writer”) and distance sensing (“the reader”). The deflection of the cantilever is measured by monitoring the heat exchange between the cantilever’s read heater and the substrate. When the cantilever encounters a feature on the surface, the heat exchange with the surface changes and consequently it either warms up or cools down. The Nanofrazor detects these changes in temperature via the change in current flowing through the heater (*i.e.* a change in resistance), transducing this signal into a surface topography. For temperature calibration, the cantilever is positioned at a constant height used for patterning. Being the heat flux with the surface constant, the temperature of the tip depends only on the applied voltage/flowing current during this calibration (essentially the I-V curve is recorded). Initially, the current grows linearly with the voltage (ohmic behavior), where the resistance is the sum of that of the cantilever and that of the internal side in the NanoFrazor electronics. The heater’s resistance has a well defined maximum that depends on the doping level [54]. For the NanoFrazor cantilever, the maximum of the resistance is at 725 °C. Knowing the position of this peak from the acquired I-V curve, the heater temperature for the full range of applied voltages is obtained assuming a linear dependence of the heater temperature on the power dissipated in the heater. The

recorded T(V) is used by the control system to measure T during the writing process. Fig. 3.3 shows the results of this calibration. Knowing this function the machine can

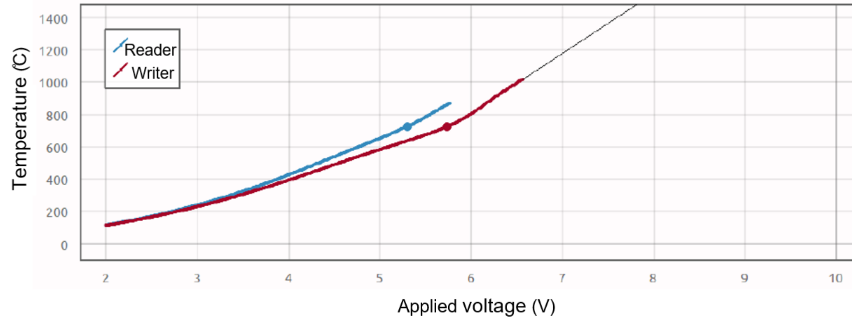

Figure 3.3: This picture shows a typical cantilever temperature curve calibration.

improve the reader's transduction capability and precisely set the appropriate voltage to the writer to achieve the desired temperature.

3.1.2. Reading

The imaging capability of the NanoFrazor provides a high-resolution topography image of the surface. This allows for the depth feedback control and the markerless alignment to pattern overlay. While reading, the tip maintains continuous contact and exerts a constant force as it is scanned over the surface. When the cantilever encounters a recess in the surface topography, it bends down due to the elastic force and the reader cools down. To achieve this, a constant voltage is applied to the heater and the current flowing through the heater is measured.

Reading mode paramaters

The machine allows to adjust some parameters to improve imaging and reduce artifacts. These parameters are:

Read height. The reading height must be adjusted according to the topography which is being imaged because if the tip moves over a sufficiently deep hole it may lose contact with the surface, since the z-piezo position is not changed within a readline. This loss of contact leads to an inaccurate measurement of the topography and artifacts like sudden jumps in the measured depth from one read line to the next one, fig. 3.4 shows this problem. The reading height should be set to match the expected maximum hole depth. When reading on resist (PPA) the maximum will in general not exceed its thickness. The zero depth is taken at the "snap-in" event, hence, we verified that the optimum value of reading height parameter is attested at about -30 nm for a 30 nm thick resist film.

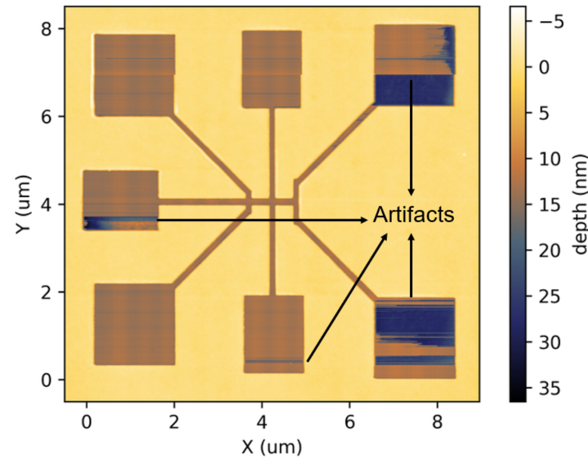

Figure 3.4: Sudden jumps in the measured depth caused by loss of contact. Reducing the reading height typically helps.

Read force. The total force exerted by the tip on the substrate surface during reading is equal to the elastic force of the cantilever. It can be estimated as $F = k\Delta z$ where k is the elastic constant of the tip (typically about 1 N/m) and Δz is the negative read height. In addition there are van der Waals forces between the tip and the surface. If the read force is too high, the PPA surface can be damaged during reading. This is of particular concern when producing high resolution patterns or using a blunt tip.

Read upsampling. The read upsampling factors for x and y controls how many read pixels are recorded for each write pixel. In order to accurately reconstruct the real surface topography, a read pixel size smaller than half of the size of the smallest expected feature should be used. Unnecessary use of high read upsampling should be avoided because it significantly reduces the throughput. Moreover, repeated reading leads to degradation of the tip and possible damage to the surface. For this work, an 1:1 ratio between read/write pixels with a pixel size between 8 to 10 nm has been used.

3.1.3. Writing

The NanoFrazor patterns a thermal resist, by bringing the heated tip of the thermal cantilever in contact with this resist material, this leads to resist sublimation. Fig. 3.5 depicts the writing process concept. The tip is scanned over the surface at a constant height called the write height. When the writer is turned ON, the cantilever bends towards the surface both as a result of the thermal bimorph effect and an electrostatic force arising from the heater voltage. When not writing, the tip is separated from the surface by the so-called write height. The depth of the patterned feature depends on both the temperature

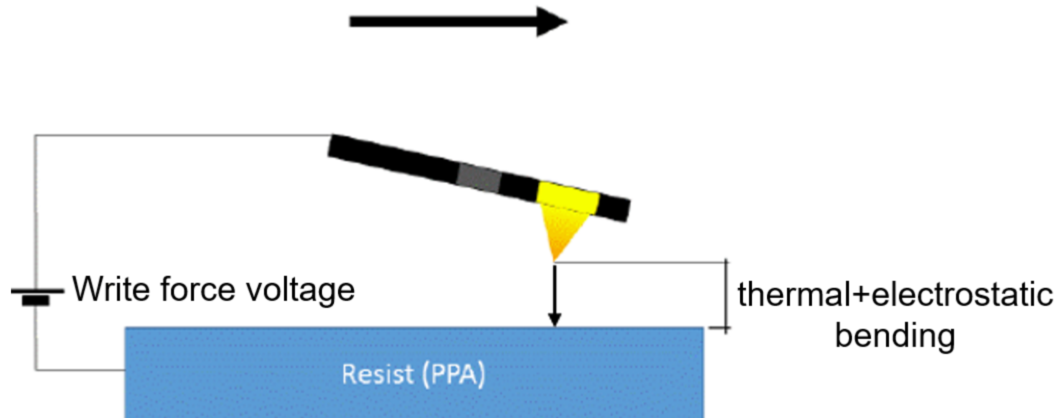

Figure 3.5: The tip scans the surface at a constant write height. The value of this write height should be set so that, when the writer voltage is turned on, the thermal plus electrostatic deflections get the tip in contact with the surface.

of the tip when it contacts the surface and the strength of the electrostatic force. The selection of parameters in writing mode follows:

Writer temperature. Polyphthalaldehyde (PPA) sublimates at less than 200 °C. However, much higher heater temperatures are required to pattern the resist, mainly because of (see section 2.2.1). Moreover, higher temperatures allow for decomposition in the microsecond timescale (the tip-sample interaction). Consequently, patterning occurs between 500 °C - 700 °C and above. Higher temperatures may allow for deeper patterning, but this comes at the expense of resolution because of the heat diffusion. When patterning on resist, the temperature should therefore be adjusted according to the target thickness and desired resolution. We observed that to successfully sublimate a 30 nm thick PPA, temperatures in the 850 °C to 1000 °C range are required.

Write height. The write height must be set to a value larger than the sum of this writer voltage deflection plus the adhesion length. If this is not the case, the tip will exert an high pressure and stick to the surface even after the electrostatic force is switched off, leading to deep indentations and artifacts. In contrast, if the write height is set too high, the tip might not reach the target depth even when the writer voltage saturates to achieve the maximum possible electrostatic force. It is important to note that write height and the temperature are the most important controllable and related parameters in the Nanofrazor, that lead to a correct sublimation depth (the target depth is equal to the PPA layer thickness, *i.e* the whole layer is removed) or to an unsuccessful patterning (a lower actual depth will prevent correct development of the pattern). Fig. 3.6 shows an extreme case in which the write height is too low and the hot tip touches the PPA surface when no

force is applied, resulting in a full removal of PPA from the scanned region instead of the transfer of the correct pattern to the resist. Typically, the cantilevers can be actuated by 300 nm although this can vary by as much as 50% within a batch of cantilevers. For this work, writing heights between 150 and 250 nm with temperatures in the range reported above achieved the best patterns.

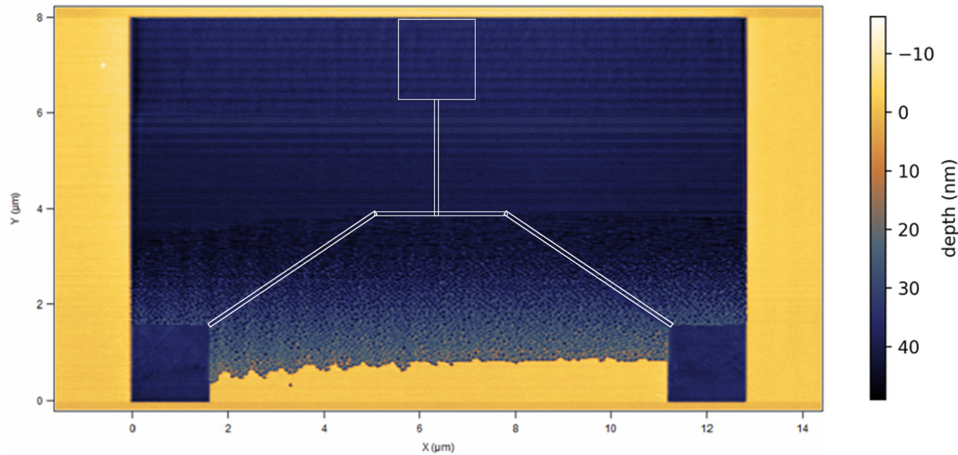

Figure 3.6: When the write height is extremely low, the NanoFrazor writes all the scanned region instead of the target pattern even though the depth feedback has already set the force to the minimum (0 V).

Force pulse duration. When the electrostatic force is switched on, the cantilever is pulled towards the surface. The resonant frequency of the cantilevers is around 150 kHz, so roughly 4 μs are required for the tip to reach the surface. Pulse durations shorter than this will not result in a written pattern. In this work, the force pulse duration was finely tuned to 10-12 μs.

Heat Pulse Duration. The writer voltage can be applied either continuously or via heat pulses, which are applied once per write pixel. This pulsed heating mode can help in reducing the wear of the cantilever by avoiding electromigration in the vicinity of the heater. The heat pulse ends at the same time as the force pulse when the tip separates from the surface. Because the thermal time constant of the cantilever is around 100 μs and as such much longer than the mechanical time constant reported above, the duration of the heat pulse must be longer than the duration of the force pulse. This allows the cantilever to warm up before touching the surface. The optimized value for this paramater in our investigation is 15 μs.

Pre-tension force. A substrate voltage can be used to bias the tip position closer to the surface before the application of the force pulse. This biasing force is called the pre-

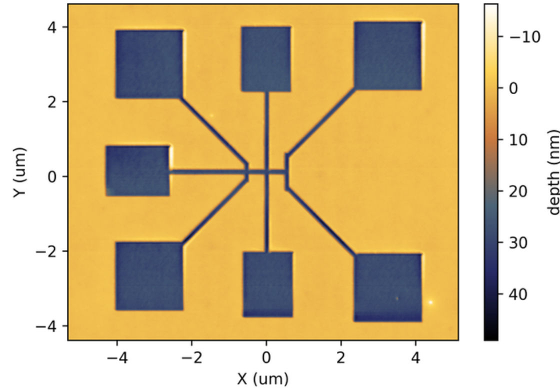

Figure 3.7: The resulting patterning achieved after optimization of both the reading and writing parameters. The actual depth is equal to PPA thickness and there are no reading artifacts.

tension force. It is switched off at the end of the force pulse. This is done to produce a higher restoring force to pull the tip off the surface after the pixel has been written. When it is desirable to reduce the force pulse below 5 μs, this pre-tension force should be used [47].

Fig. 3.7 reports the pattern achieved after fine tuning the reading and writing parameters: no artifacts are present and measured depth is equal to the PPA thickness. It's important to note that the optimal value of such parameters might vary when patterning different layouts or working directly on a bare substrate.

Depth feedback

The amount of resist removed by the NanoFrazor at each point can be controlled via the force applied to the cantilever [55]. The depth feedback exploits the *in-situ* reading capability to adjust the electrostatic force applied during patterning in real time. Before patterning, an initial estimate of the voltage required to achieve the desired write depth is done. After each line is written in the forward direction, the reader scans the topography in the backward direction. The depth feedback examines the written depth and uses this information to improve the estimate of the force voltages for the next write line. The depth feedback increases the electrostatic force when the measured depth is lower than the target depth, and decreases it when the measured depth is higher than the target depth. This closed loop lithography concept allows for 3D grayscale patterning, in which the target depth varies line by line. The machine features a PID and Kalman feedback loop controls, the Kalman performs better.

3.1.4. Description of a complete lithographic process

The procedure begins with the loading of the GDS layout into the Nanofrazor software. This layout represents the design to be transferred to the resist. The hybrid nature of the machine (t-SPL/optical) will be exploited. This means that the layout is divided in two main sectors, as can be seen from Fig. 3.8a. The core of the structure (enclosed by a circle in the picture) comprises a nanometric pattern transferred by t-spl. The larger features (in the order of 2μm) which are optically feasible are patterned with the laser in order to minimize the tip degradation and increase the throughput. The importation tool in the software allows to define a target depth for each sector, which is called *field*, together with the pixel size dx dy in nm. The pixel size determines how much the tip or laser will move on the surface at every step. Each *field* can independently be assigned to t-SPL or laser with a different pixel size. The alignment procedure between physical and optical fields is not straightforward. In principle, it should be possible to align isolated t-SPL features with a laser field, but there are some intrinsic complications in this process. The laser's coordinate system would have to be calibrated to match the the reference frame of the piezo scanner, because the laser is not integrated in the cantilever. So that when one is patterning a layout with hybrid fields (thermal/optical), the laser features would connect with the t-SPL ones. To achieve this, the NanoFrazor features an algorithm to estimate the relative offset between the "zero" of the tip and that of the laser in the plane. Unfortunately, the automatic procedure for the determination of the offset provided by the machine is far from perfect. The improvement of this procedure requires software modifications by *Heidelberg*. Being unable to reliably proceed with the automatic alignment, I found a different way to overcome this limitation. Fig. 3.8c shows that as a matter of fact is possible to write the laser fields first and then align the t-SPL ones with good precision by exploiting the capability of the tip to do the imaging and thus a precise alignment. As Fig. 3.8b shows, if the image of the optically exposed parts is acquired then it results easily to overlay the t-SPL topography in the desired position. The same flawless alignment concept is applied again when creating overlays in subsequent steps of the process, as explained in section 3.2.3.

Throughput

One of the challenges of t-SPL is the limited throughput (see section 2.2.1). The time required to pattern a single structure with the NanoFrazor drastically depends on the pixel size, the upsampling factor and the total scanned area. We noticed that the scanning speed depends on the pixel size alone, both for writing and reading (*i.e.* the time required to write or read a given area is the same). If the upsampling factor is increased in one

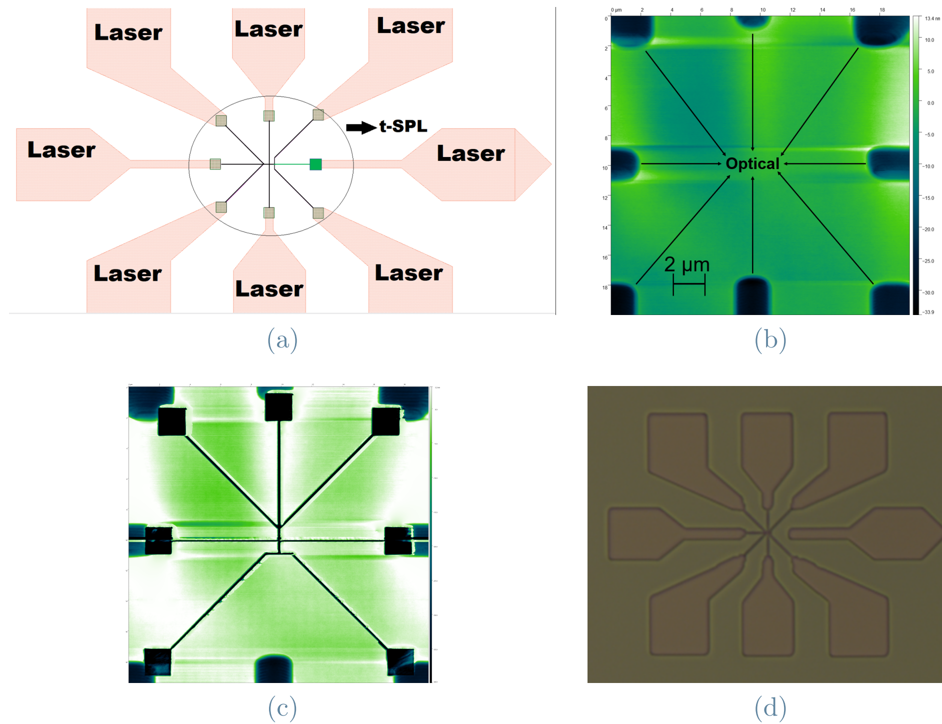

Figure 3.8: **(a)** A sketch of the layout with the different lithographic fields. **(b)** Reading mode image after patterning with the laser. **(c)** t-SPL field aligned with the optical ones. **(d)** Optical microscope image of the developed patterns.

direction (*e.g.* 1:2) the total time doubles because the tip reads more pixels, even if the layout is the same. The total scanned area is fixed by the layout. As explained above, we worked with a pixel size of about 8 to 10 nm and 1:1 upsampling factor, this resulted in a total writing time of about 10 minutes on a 19x19 μm area ($\sim$ 3000 $\times$ 3000 pixels, see Fig. 3.8c). It's important to note that this time includes delays introduced by the electronics and the software.

3.2. The bilayer lift-off process

The bilayer lift-off process is a t-SPL pattern transfer technique which features a double polymer resist stack. During the writing procedure, the tip sublimates a thin thermal resist layer on top of a lift-off resist layer (see Fig. 3.9a). With regards to an optimal positive thermal resist, high sensitivity to heat is key. Polyphthalamide (PPA) is the current gold standard for t-SPL. The PPA layer is spun on top a lift-off resist which in this work was a copolymer composed of methyl methacrylate and methacrylic acid (PMMA/MA). PMMA/MA is normally employed for high resolution e-beam lithography and in t-SPL it's not directly thermally activated by the tip during writing. The pattern

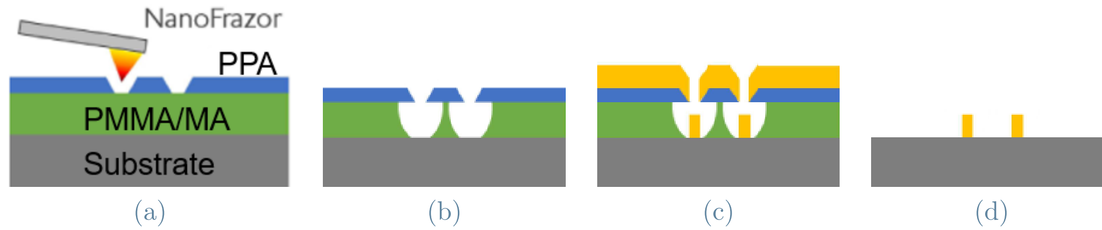

Figure 3.9: **(a)** The NanoFrazor tip imprints a pattern by locally sublimating the thermal resist PPA. **(b)** The sample is developed in a solution and the pattern is transferred in the lift-off resist layer PMMA; wet isotropic processes lead to the so called "undercut". **(c)** A metallic thin film is deposited. **(d)** Finally, the sample is immersed in a proper solvent to strip the residual resist layers. As a result, the metallic pattern is formed on the substrate.

transfer from PPA to the lift-off resist below is carried out with a development procedure in which the PMMA/MA is wet etched in solution. The etching process is isotropic and this results in an undercut profile (Fig. 3.9b). After development, the latent image is imprinted on both layers and used as a mask for additive or subtractive processes (Fig. 3.9c). Later, both the resist layers can then be stripped in a polar solvent such as acetone (Fig. 3.9d). The bilayer lift-off can be repeated to pattern overlays (see Fig.3.10).

This double resist stack is an unique characteristic of this process, the PMMA acts as a buffer layer to allow a very uniform coating of the thermally active resist PPA, which wouldn't be possible on the bare substrate. Moreover, if the PMMA layer is thick enough (>50 nm), the substrate thermal conductivity and heat capacity do not play a role in the heat diffusion model from the tip (see section 2.2.1). This process is claimed to be limited to a resolution of 100-120 nm and above by Heidelberg, but we noticed that it's not straightforward to reach 100 nm with a certain degree of reproducibility. The next paragraphs will explore in detail the difficulties intrinsic in each step and the solutions we have found.

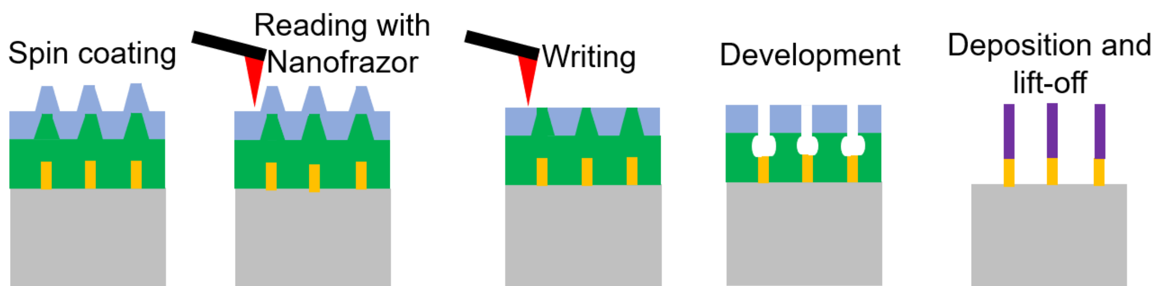

Figure 3.10: The bilayer lift-off process is repeated.

3.2.1. Details and optimization

Polyphthalamide (PPA)

PPA is employed as a thermal positive resist thanks to its susceptibility to heat. Ideally when the polymer is exposed to sufficient heating provided by the tip it should directly sublimate into its volatile monomers without leaving any residues. PPA features self-amplified decomposition which happens as a complete unzipping of the polymer backbone upon a single heat triggered bond break [56]. In addition, the unzipping reaction is endothermic which results in highly localized decomposition [57]. Macroscopically, the decomposition temperature of pure PPA lies in the same range as its glass transition temperature $T_{dec} \sim 180°$. Therefore, once the chains get mobile, they start to decompose into volatile monomers. PPA can be spin-coated in a broad thickness range of 2 nm to 10 μm and the achievable resolution is a strong function of this thickness. The Nanofrazor's tip is extremely sharp but, due to the conical shape, the deeper the patterns are, the broader they become (see fig. 3.11). Moreover, a thinner PPA allows to write with lower tip temperatures, and this also leads to a better resolution.

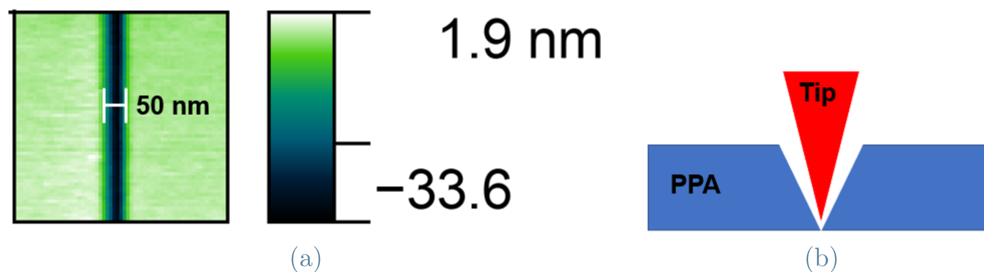

(a) (b)

Figure 3.11: **(a)** Nanofrazor's reading of a 50 nm line in which the depth profile recalls the conical shape of the tip; **(b)** larger PPA thicknesses result in a wider indentation.

The polymer is very stable if stored as a powder in a freezer for more than 1 year. However, it lasts about 1 month in solution if properly stored in a refrigerator. A degraded PPA is not flat after spinning but has valleys and mountains, and its roughness prevents the successful application of t-SPL. It is very important to always check with the Nanofrazor's imaging that the mean thickness of the resist is close to zero after spinning. We observed that variations of less than 10 % of the total PPA thickness are expected and not problematic. Picture 3.12 shows the comparison between pristine and degraded PPA layers.

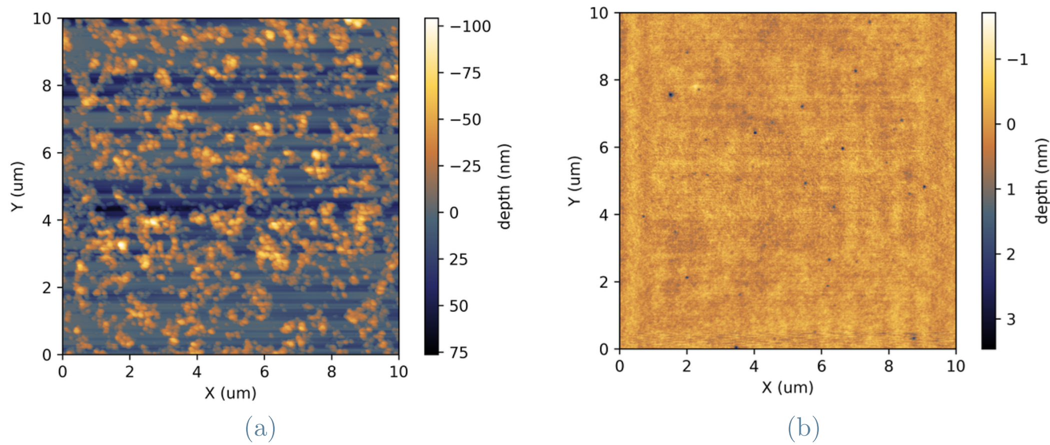

(a) (b)

Figure 3.12: **(a)** degraded PPA; **(b)** pristine PPA.

Development

After patterning the PPA with the Nanofrazor either with t-SPL or laser mode, the exposed PMMA/MA can be dissolved in a wet mixture of deionized water and isopropanol alcohol (IPA). The portion of water controls the development rate, normally a 5 % deionized water in IPA solution is prepared. The development rate in this solution was estimated to be between 1 and 1.2 nm/s by AFM measurements. The development rate can be affected by how the sample is manually stirred during development in the becker. Moreover, the absorption of water from an extended exposure of the sample to the atmosphere should be avoided as it might reduce development time. Under-developed samples characterized by PMMA/MA residuals attached to the substrate at the bottom of the patterned holes, as shown in Fig. 3.13. Considering the intrinsic variance and the multi-

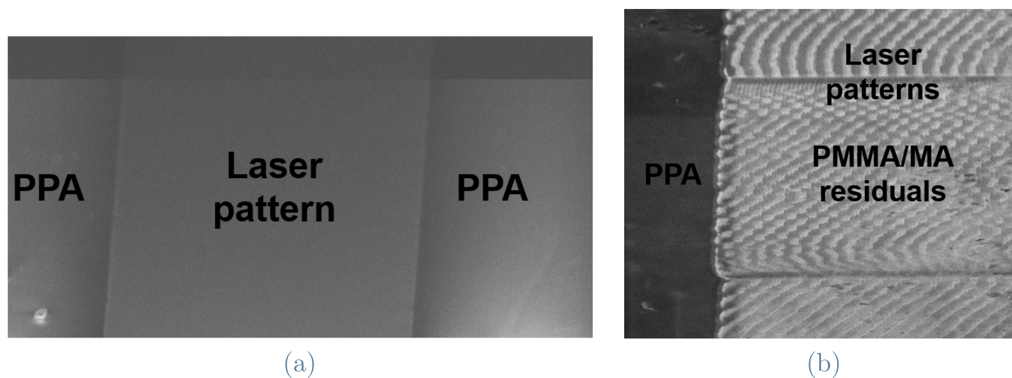

(a) (b)

Figure 3.13: **(a)** Optimal development (no residual PMMA/MA); **(b)** under-developed sample.

ple factors influencing the development time, it's always advised to check the sample with

AFM after developing.

Combining NanoFrazor lithography with the bilayer lift-off process offers a very gentle nanofabrication technique in which sample heating and damage by charged particles is avoided. However, being the etch isotropic, an undercut of the PMMA/MA at the edges of the exposed parts develops under the PPA. The rate of undercut formation is between 0.5 nm/s and 0.6 nm/s, it can be estimated by firstly patterning a matrix of lines with the NanoFrazor and then reading it after development (see Fig. 3.14). This allows to precisely determine the difference between the patterning width and the resulting developed width of each line. As we can see from this test (see table 3.1), the variance of the development rate is considerable even on the same sample. Undercut formation limits the resolution

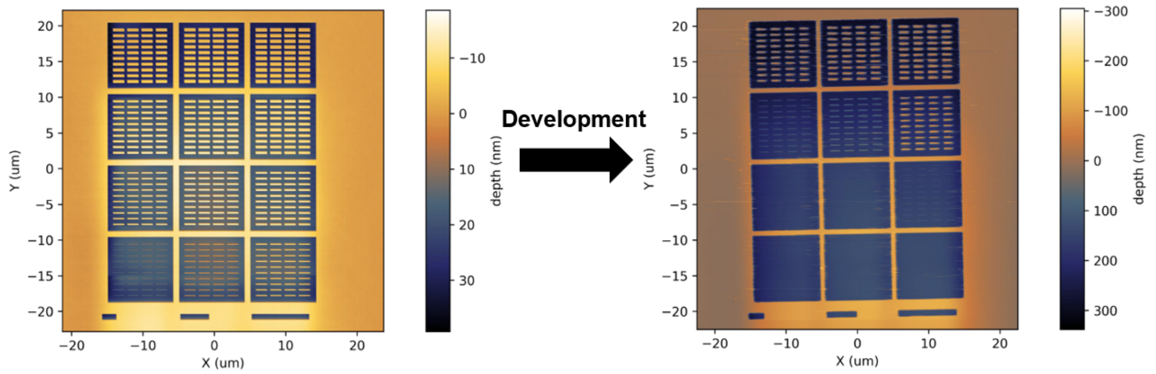

Figure 3.14: Development rate test done by *Heidelberg Instruments* on a PPA (30)/PPMA (270) stack.

Initial structure width (nm)	Remaining width (nm)
≤ 200	/
240	30
280	60
320	120
360	270
400	290
440	295
480	290

Table 3.1: Results of the development test. The undercut rate in each line is calculated as $r = \frac{I-F}{t}$ where I is the initial width, F the remaining width and t is development time. The estimated rate is 0.55 ±0.17 nm/s.

of this process: the resulting metal lines will be wider and the minimum spacing between nearby features is restricted to around twice the thickness of the lift-off resist. In this

sense, reducing the thickness of both PMMA and PPA could represent a very fruitful way of improving the minimum features of the structure (more information in the next section).

Deposition and lift-off

After the development, the sample undergoes metal deposition by either sputtering or e-beam evaporation. Finally, to "lift-off" the unwanted parts of the film, the sample is immersed in a proper solvent (*e.g.* acetone or DMSO) which dissolves the residual resist. One may first remove the excess metal before the lift-off by stripping a piece of kapton tape gently against the deposited film and peeling it off gently. Most of the metal film should attach to the piece of tape and this eases the lift-off by increasing the contact area of the solvent and reducing re-deposition of metal flakes.

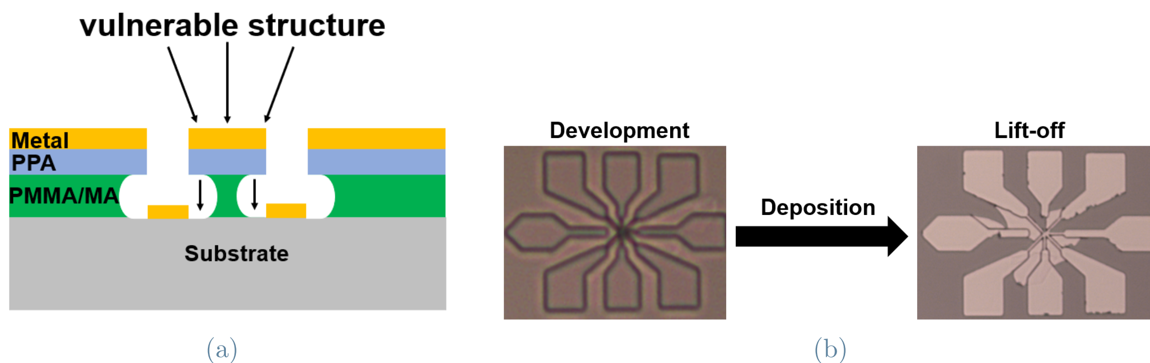

Figure 3.15: **(a)** a weak point in the structure that can lead to resist collapse. **(b)** an example of a bad lift-off.

We observed that the undercut formation during development might cause mechanical instability in some vulnerable structures as can be seen in Fig. 3.15a. This mechanical instability can lead to a collapse of the resist stack in between undercuts of nearby features when depositing the metal or during lift-off. Fig. 3.15b shows a microscope image of a sample before deposition and after lift-off: the development of the structure is clearly successful and this was confirmed with AFM measurements, meaning that the patterned holes depth were exactly equal to the whole resist stack height; after metal deposition and lift-off, the features were compromised and this might be caused by the adhesion of metal where the resist collapses. We observed bad lift-offs on more than 20 samples (either with or without tape), and it was later confirmed by *Heidelberg* (private talk) that it may be caused by the mechanical instability of the resist stack.

3.2.2. Strategies to improve the resolution with a resist-based approach

In order to push the resolution of this process and improving the lift-off yield we followed an optimization procedure on the PMMA/MA layer. A thinner PMMA requires less development time, hence reducing the undercut and improving both the resolution and the structural stability. We had lift-off problems (see Fig. 3.15) on a lot of samples with standard 110 to 120 nm thick films of *AR-P 610.03* PMMA/MA from *Allresist* with 3% solid content, spinned at 4000 rpm. Moreover, the initial resolution was not suitable to achieve the objectives of this thesis, due to the fact that the resulting Pt structures had a minimum feature size of 120 and above. One can adjust the thickness of the PMMA/MA by diluting it with a solvent (*e.g.* PGME) and/or by spinning it faster. To mitigate these issues, we followed a meticulous optimization approach on the thickness of PMMA layer. The spinning speed was increased to 6000 rpm and this resulted in a thinner PMMA of

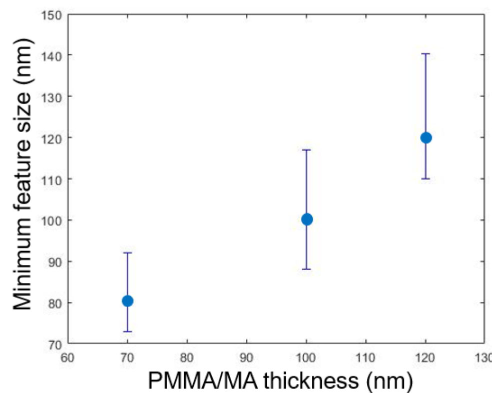

Figure 3.16: Optimization of the thickness of the PMMA/MA layer. The points indicate the mean.

about 100 nm. Then, the resist was diluted with PGME to reach 1% solid content. The dilution led to a 65 to 70 nm thick PMMA/MA. This improved the lift-offs yield and allowed to reach a resolution of about 80 nm (see Fig. 3.16).

3.2.3. Fabrication of the nanostructures

This section shows the results obtained by applying the optimized bilayer lift-off process to obtain the nanostructures described at the beginning of this chapter.

Heavy Metal Structure Definition

At first the two polymer layers are spin coated on the sample: $\sim$ 70 nm of PMMA/MA beneath 30 nm of PPA. The desired thickness is achieved in this case with the following spin coating recipe: 6000 rpm for 60 seconds for the PMMA/MA (1% solid content) and 4000 rpm for the PPA layer. A standard soft bake procedure on hot plate follows after each resist is spun on the substrate. The soft bake is necessary to make the solvent evaporate, this is achieved by heating the sample at about 180 °C for PMMA and at 110 °C for PPA, for 90 seconds. The desired pattern is then imprinted on the PPA layer with the NanoFrazor. Fig. 3.17b shows an AFM image of the t-SPL patterning. To transfer the image of the desired geometry to the PMMA/MA, the sample is then developed by immersion in a solution of isopropyl alcohol (IPA) and water (20:1) for about 70 seconds (1 nm/s). A 5 to 10 nm thin-film of heavy metal (Pt/ Ta) is then deposited by magnetron sputtering deposition (AJA) or e-beam evaporation. The deposition techniques achieved comparable results. Finally, the sample is immersed in a strong solvent such as acetone and both the lift-off resist and the thermal resist are stripped. The geometry patterned in PPA is finally transferred to the deposited material. Figure 3.17c shows an AFM image of the device after this step. It's important to note that the t-SPL technique is employed in this step to pattern the smaller features which require nanometric resolution as can be seen in picture 3.17b. Meanwhile, the laser integrated in the NanoFrazor is used for the portion of the layout which can be done with an optical tool (see Fig. 3.8 for reference). Both t-SPL and laser parts are written and developed on the same resist.

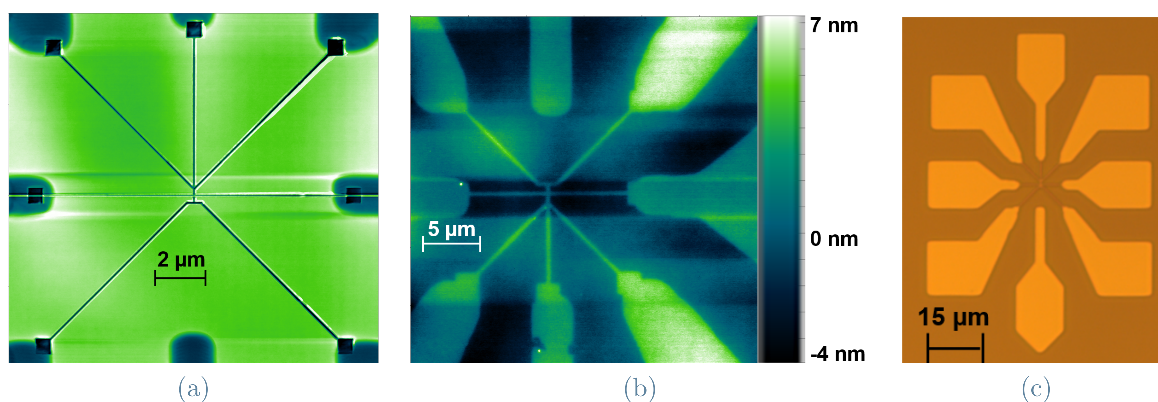

(a) (b) (c)

Figure 3.17: NanoFrazor *in-situ* reading of the t-SPL patterning.**(b)** The structure after lift-off.**(c)** Optical microscope image of the device after this step.

Magnetic layer

At this point, the bilayer lift-off process is repeated to fabricate the ferromagnetic electrode which injects the spin-polarized current within the previously deposited SOC structure. Both the lift-off resist and the thermal one are spin coated again on the sample with the same recipe. Exploiting the integrated reading of the NanoFrazor, it's possible to align and to write a nanometric magnetic pillar on top of the first layer in the desired position (see Fig. 3.18). After this reading and writing procedure has been repeated for every

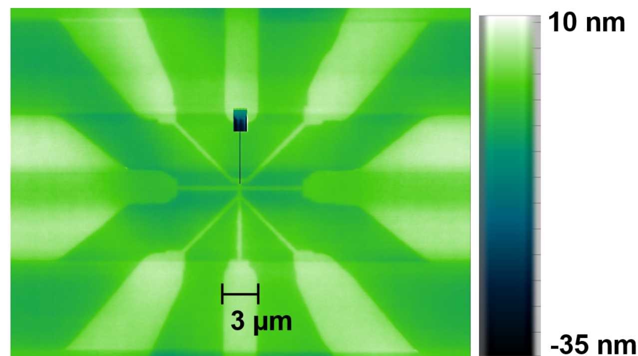

Figure 3.18: The Nanofrazor's reading and writing procedure allows to align the magnetic pillar on top of Pt exactly in the desired position and without any markers.

structure, the sample is developed and a thin film of ferromagnetic material is deposited. With reference to the results of Pham *et al.* [10], the thickness of the ferromagnet should be greater than that of the non-magnet. As a rule of thumb, the target thickness of this layer should be $t_{FM} \sim 2t_{NM}$. This deposition can be carried out both with the e-beam evaporator (NiFe) or with magnetron sputtering (CoFeB). Fig. 3.19 shows the image of the device after this step.

Output Contacts

In the last step optical lithography is employed to make output contacts. A light sensitive photoresist (*AZ5214E*) is used. The thickness of about 1.4 μm is obtained by spinning at 6000 rpm for 60 seconds. A soft bake is performed, at about 110 °C for 90 seconds. The sample is then exposed with MLA (see section 2.2.2) with a dose of 30 mJ/cm^2, aligning the pattern with the Nanofrazor's lithography using a series of crosses made on purpose during the first step.

After exposure, a reversal bake for 90 seconds at 115°C is performed, followed by a flood exposure for 120 seconds, under UV light, to obtain undercut profiles. The development procedure in the case of *AZ5214E* photoresist consists in 30 s immersion in *AZ 726MIF*,

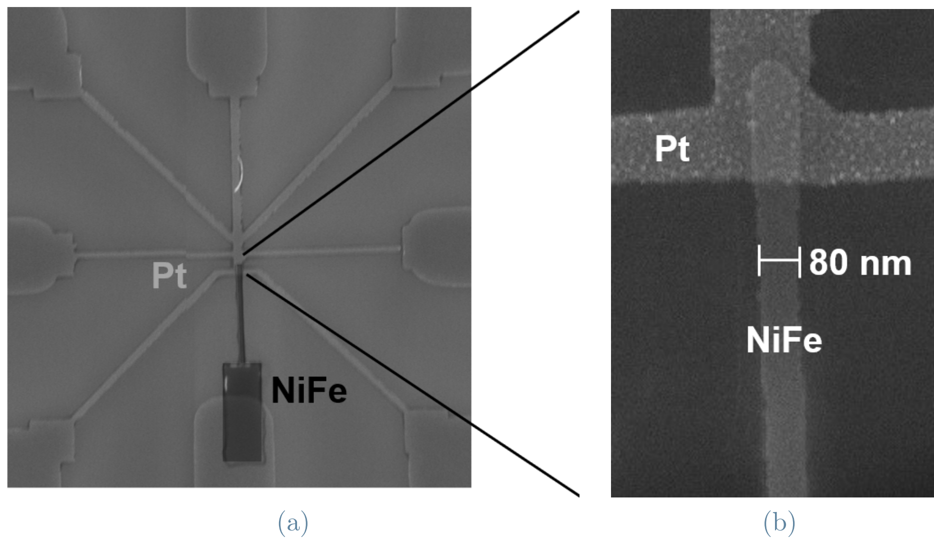

(a) (b)

Figure 3.19: **(a)** SEM image of the finalized nanostructure, **(b)** higher magnification image.

followed by rinse in water. The desired stack of contacts materials Cr(10)/Cu(100)/Au(50) are evaporated with a thermal evaporation tool (Moorfield). A standard lift-off step in acetone follows. The thickness of the metal in these output contacts is enough to withstand measurement probe landings or bonding. Fig. 3.20 shows the finalized device.

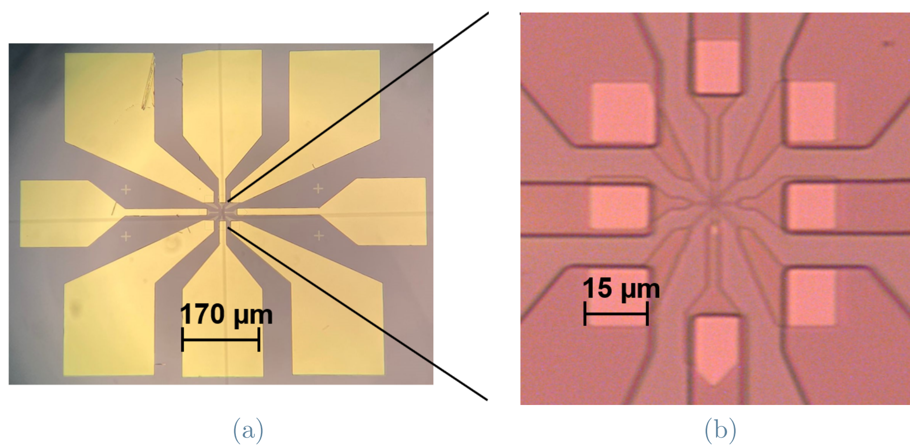

(a) (b)

Figure 3.20: **(a)** Optical microscope image of the finalized device complete with evaporated noble metal output contacts; **(b)** higher magnification image.

We tried to perform the measurements on the fabricated nanostructures as explained at the beginning of this chapter. The resistivity measurements on the Pt core worked as intended: we managed to injected a current and measure a voltage. However, there

was a problem with the nanomagnets. Even if the structures appeared to be physically connected with the Pt, there was no electrical continuity when we tried to injected a current in the nanomagnet. This might be due to the oxidation of the ~ 10 nm thick magnets caused by the solvents for optical lithography. A capping layer should be added in order to prevent this oxidation.

Conclusions and perspectives

The objective of this thesis was to reach 50 nm resolution with t-SPL and a solely resist-based approach, motivated by the perspective to realize spin-orbit based devices exploiting thermal nanolithography. The practical operation of the Nanofrazor was studied in detail to achieve the best possible patterns and solve the alignment issues arising when both t-SPL and optical writing are used to achieve multiscale designs. Such work of optimization of the bilayer lift-off process has required a significant effort and number of samples but allowed to unveiled the peculiar issues arising when the resolution goes below standard limits (role of the undercut in features broadening, mechanical instability of the resist stack, etc.). While extreme care on the physics of the process is needed when fabricating with t-SPL, we succeed in mastering the technique pushing the resolution down to 80 nm while improving reliability, by thinning the resist layer. Noteworthy, we identified that the critical dimension of the lithography process is roughly equal to the thickness of the resist. Thus, further thinning of the resist is expected to allow for 50 nm resolution and beyond. In perspective, we foresee that resolution could be pushed in the 20 to 30 nm range with the bilayer lift-off process, employing a PPA of about 10 nm and a PMMA of about 40 nm. Moreover, the acquired knowledge on the practical operation of the NanoFrazor and the bilayer lift-off process will be essential in the future in view of the use of 2D materials or thin films of FERSC that could be damaged by more invasive processes.

Bibliography

[1] Sasikanth Manipatruni, Dmitri E Nikonov, and Ian A Young. Beyond cmos computing with spin and polarization. *Nature Physics*, 14(4):338–343, 2018.

[2] Sasikanth Manipatruni, Dmitri E Nikonov, Chia-Ching Lin, Tanay A Gosavi, Huichu Liu, Bhagwati Prasad, Yen-Lin Huang, Everton Bonturim, Ramamoorthy Ramesh, and Ian A Young. Scalable energy-efficient magnetoelectric spin–orbit logic. *Nature*, 565(7737):35–42, 2019.

[3] Nicola Jones et al. The information factories. *Nature*, 561(7722):163–6, 2018.

[4] Mark Horowitz. 1.1 computing's energy problem (and what we can do about it). In *2014 IEEE International Solid-State Circuits Conference Digest of Technical Papers (ISSCC)*, pages 10–14. IEEE, 2014.

[5] Axel Hoffmann. Spin hall effects in metals. *IEEE transactions on magnetics*, 49(10):5172–5193, 2013.

[6] Victor M Edelstein. Spin polarization of conduction electrons induced by electric current in two-dimensional asymmetric electron systems. *Solid State Communications*, 73(3):233–235, 1990.

[7] Christian Rinaldi, JC Rojas-Sánchez, RN Wang, Y Fu, S Oyarzun, L Vila, Stefano Bertoli, Marco Asa, Lorenzo Baldrati, Matteo Cantoni, et al. Evidence for spin to charge conversion in gete (111). *APL Materials*, 4(3):032501, 2016.

[8] LL Tao and Evgeny Y Tsymbal. Perspectives of spin-textured ferroelectrics. *Journal of Physics D: Applied Physics*, 54(11):113001, 2021.

[9] Christian Rinaldi, Sara Varotto, Marco Asa, Jagoda Slawinska, Jun Fujii, Giovanni Vinai, Stefano Cecchi, Domenico Di Sante, Raffaella Calarco, Ivana Vobornik, et al. Ferroelectric control of the spin texture in gete. *Nano letters*, 18(5):2751–2758, 2018.

[10] Inge Groen, Sasikanth Manipatruni, Won Young Choi, Dmitri E Nikonov, Edurne Sagasta, Chia-Ching Lin, Tanay A Gosavi, Alain Marty, Luis E Hueso, Ian A Young,

et al. Spin–orbit magnetic state readout in scaled ferromagnetic/heavy metal nanostructures. *Nature Electronics*, 3(6):309–315, 2020.

[11] Nevill Francis Mott. The electrical conductivity of transition metals. *Proceedings of the Royal Society of London. Series A-Mathematical and Physical Sciences*, 153(880):699–717, 1936.

[12] T Valet and AJPRB Fert. Theory of the perpendicular magnetoresistance in magnetic multilayers. *Physical Review B*, 48(10):7099, 1993.

[13] Tai L Chow. *Introduction to electromagnetic theory: a modern perspective*. Jones & Bartlett Learning, 2006.

[14] David J Griffiths and Darrell F Schroeter. *Introduction to quantum mechanics*. Cambridge university press, 2018.

[15] Ludwig Föppl and Perrey Daniell. Zur kinematik des bornschen starren körpers. *Nachrichten von der Gesellschaft der Wissenschaften zu Göttingen, Mathematisch-Physikalische Klasse*, 1913:519–529, 1913.

[16] Jairo Sinova, Sergio O Valenzuela, Jörg Wunderlich, CH Back, and T Jungwirth. Spin hall effects. *Reviews of Modern Physics*, 87(4):1213, 2015.

[17] Mikhail I D'Yakonov and VI Perel. Possibility of orienting electron spins with current. *ZhETF Pisma Redaktsiiu*, 13:657, 1971.

[18] Robert Karplus and JM Luttinger. Hall effect in ferromagnetics. *Physical Review*, 95(5):1154, 1954.

[19] Naoto Nagaosa, Jairo Sinova, Shigeki Onoda, Allan H MacDonald, and Nai Phuan Ong. Anomalous hall effect. *Reviews of modern physics*, 82(2):1539, 2010.

[20] Michel I Dyakonov and AV Khaetskii. Spin hall effect. In *Spin physics in semiconductors*, pages 211–243. Springer, 2008.

[21] T Seki, I Sugai, Y Hasegawa, S Mitani, and K Takanashi. Spin hall effect and nernst effect in fept/au multi-terminal devices with different au thicknesses. *Solid State Communications*, 150(11-12):496–499, 2010.

[22] Yuan Tian, Li Ye, and Xiaofeng Jin. Proper scaling of the anomalous hall effect. *Physical review letters*, 103(8):087206, 2009.

[23] Atsuo Shitade and Naoto Nagaosa. Anomalous hall effect in ferromagnetic metals: Role of phonons at finite temperature. *Journal of the Physical Society of Japan*, 81(8):083704, 2012.

[24] Nevill Francis Mott, Harrie Stewart Wilson Massey, and The International Series of Monographs on Physics. *The theory of atomic collisions*, volume 35. Clarendon Press Oxford, 1965.

[25] Martin Gradhand, Dmitry V Fedorov, Peter Zahn, and Ingrid Mertig. Extrinsic spin hall effect from first principles. *Physical review letters*, 104(18):186403, 2010.

[26] Luc Berger. Side-jump mechanism for the hall effect of ferromagnets. *Physical Review B*, 2(11):4559, 1970.

[27] Albert Fert and Peter M Levy. Spin hall effect induced by resonant scattering on impurities in metals. *Physical review letters*, 106(15):157208, 2011.

[28] T Tanaka, Hiroshi Kontani, Masayuki Naito, T Naito, Dai S Hirashima, K Yamada, and J Inoue. Intrinsic spin hall effect and orbital hall effect in 4 d and 5 d transition metals. *Physical Review B*, 77(16):165117, 2008.

[29] Hiroshi Kontani, T Tanaka, DS Hirashima, K Yamada, and J Inoue. Giant orbital hall effect in transition metals: Origin of large spin and anomalous hall effects. *Physical review letters*, 102(1):016601, 2009.

[30] Gene Dresselhaus. Spin-orbit coupling effects in zinc blende structures. *Physical Review*, 100(2):580, 1955.

[31] Junsaku Nitta, Tatsushi Akazaki, Hideaki Takayanagi, and Takatomo Enoki. Gate control of spin-orbit interaction in an inverted i n 0.53 g a 0.47 as/i n 0.52 a l 0.48 as heterostructure. *Physical Review Letters*, 78(7):1335, 1997.

[32] K Ishizaka, MS Bahramy, H Murakawa, M Sakano, T Shimojima, T Sonobe, K Koizumi, S Shin, H Miyahara, A Kimura, et al. Giant rashba-type spin splitting in bulk bitei. *Nature materials*, 10(7):521–526, 2011.

[33] YC Cheng, ZY Zhu, Muhammad Tahir, and Udo Schwingenschlögl. Spin-orbit–induced spin splittings in polar transition metal dichalcogenide monolayers. *EPL (Europhysics Letters)*, 102(5):57001, 2013.

[34] Van Tuong Pham, Laurent Vila, Gilles Zahnd, Alain Marty, Williams Savero-Torres, Matthieu Jamet, and Jean-Philippe Attane. Ferromagnetic/nonmagnetic nanostructures for the electrical measurement of the spin hall effect. *Nano letters*, 16(11):6755–6760, 2016.

[35] JC Sánchez, Laurent Vila, G Desfonds, S Gambarelli, JP Attané, JM De Teresa,

C Magén, and A Fert. Spin-to-charge conversion using rashba coupling at the interface between non-magnetic materials. *Nature communications*, 4(1):1–7, 2013.

[36] AR Mellnik, JS Lee, A Richardella, JL Grab, PJ Mintun, Mark H Fischer, Abolhassan Vaezi, Aurelien Manchon, E-A Kim, Nitin Samarth, et al. Spin-transfer torque generated by a topological insulator. *Nature*, 511(7510):449–451, 2014.

[37] CK Safeer, Josep Ingla-Aynés, Franz Herling, José H Garcia, Marc Vila, Nerea Ontoso, M Reyes Calvo, Stephan Roche, Luis E Hueso, and Fèlix Casanova. Room-temperature spin hall effect in graphene/mos2 van der waals heterostructures. *Nano letters*, 19(2):1074–1082, 2019.

[38] E Lesne, Yu Fu, S Oyarzun, JC Rojas-Sánchez, DC Vaz, H Naganuma, G Sicoli, J-P Attané, M Jamet, E Jacquet, et al. Highly efficient and tunable spin-to-charge conversion through rashba coupling at oxide interfaces. *Nature materials*, 15(12):1261–1266, 2016.

[39] Yu Kyoung Ryu Cho, Colin D Rawlings, Heiko Wolf, Martin Spieser, Samuel Bisig, Steffen Reidt, Marilyne Sousa, Subarna R Khanal, Tevis DB Jacobs, and Armin W Knoll. Sub-10 nanometer feature size in silicon using thermal scanning probe lithography. *ACS nano*, 11(12):11890–11897, 2017.

[40] Donald M Mattox. Physical vapor deposition (pvd) processes. *Metal Finishing*, 100:394–408, 2002.

[41] James D Plummer and Peter B Griffin. Material and process limits in silicon vlsi technology. *Proceedings of the IEEE*, 89(3):240–258, 2001.

[42] Martin Knudsen. Die verdampfung von kristalloberflächen. *Annalen der Physik*, 357(1):105–108, 1917.

[43] Francis Weston Sears, Gerhard L Salinger, and John E Lee. *Thermodynamics, kinetic theory, and statistical thermodynamics*. Addison-Wesley, 1975.

[44] Samuel Tobias Howell, Anya Grushina, Felix Holzner, and Juergen Brugger. Thermal scanning probe lithography—a review. *Microsystems & Nanoengineering*, 6(1):1–24, 2020.

[45] Xiaorui Zheng, Annalisa Calò, Edoardo Albisetti, Xiangyu Liu, Abdullah Sanad M Alharbi, Ghidewon Arefe, Xiaochi Liu, Martin Spieser, Won Jong Yoo, Takashi Taniguchi, et al. Patterning metal contacts on monolayer mos2 with vanishing schottky barriers using thermal nanolithography. *Nature Electronics*, 2(1):17–25, 2019.

[46] Eric M Panning and Martha I Sanchez. Novel patterning technologies. In *Proc. of SPIE Vol*, volume 10584, pages 1058401–1, 2018.

[47] Philip C Paul, Armin W Knoll, Felix Holzner, Michel Despont, and Urs Duerig. Rapid turnaround scanning probe nanolithography. *Nanotechnology*, 22(27):275306, 2011.

[48] Peter Vettiger, G Cross, M Despont, U Drechsler, U Durig, B Gotsmann, W Haberle, MA Lantz, HE Rothuizen, R Stutz, et al. The" millipede"-nanotechnology entering data storage. *IEEE Transactions on nanotechnology*, 1(1):39–55, 2002.

[49] William P King, Bikramjit Bhatia, Jonathan R Felts, Hoe Joon Kim, Beomjin Kwon, Byeonghee Lee, Suhas Somnath, and Matthew Rosenberger. Heated atomic force microscope cantilevers and their applications. *Annual Review of Heat Transfer*, 16, 2013.

[50] Brent A Nelson and William P King. Modeling and simulation of the interface temperature between a heated silicon tip and a substrate. *Nanoscale and Microscale Thermophysical Engineering*, 12(1):98–115, 2008.

[51] Jungchul Lee, Tanya L Wright, Mark R Abel, Erik O Sunden, Alexei Marchenkov, Samuel Graham, and William P King. Thermal conduction from microcantilever heaters in partial vacuum. *Journal of applied physics*, 101(1):014906, 2007.

[52] K Luo, Z Shi, J Varesi, and A Majumdar. Sensor nanofabrication, performance, and conduction mechanisms in scanning thermal microscopy. *Journal of Vacuum Science & Technology B: Microelectronics and Nanometer Structures Processing, Measurement, and Phenomena*, 15(2):349–360, 1997.

[53] Marc J Madou. *Manufacturing techniques for microfabrication and nanotechnology*. CRC press, 2011.

[54] U Dürig. Fundamentals of micromechanical thermoelectric sensors. *Journal of Applied Physics*, 98(4):044906, 2005.

[55] Armin W Knoll, David Pires, Olivier Coulembier, Philippe Dubois, James L Hedrick, Jane Frommer, and Urs Duerig. Probe-based 3-d nanolithography using self-amplified depolymerization polymers. *Advanced Materials*, 22(31):3361–3365, 2010.

[56] Hiroshi Ito and C Grant Willson. Chemical amplification in the design of dry developing resist materials. *Polymer Engineering & Science*, 23(18):1012–1018, 1983.

[57] Minoru Tsuda, Masayuki Hata, RIE Nishida, and Setsuko Oikawa. Acid-catalyzed

degradation mechanism of poly (phthalaldehyde): Unzipping reaction of chemical amplification resist. *Journal of Polymer Science Part A: Polymer Chemistry*, 35(1):77–89, 1997.

List of Figures

1 Beyond-CMOS "Wheel of technologies" for state retention, state sensing, state switching and interconnects . . . 2

1.1 **(a)** MESO device formed with a magnetoelectric capacitor and a high SOC material stacked with a nanomagnet for state retention. The magnetoelectric transfer function in **(b)** shows how an input current can change the magnetization direction of the ferromagnet, displaying the typical hysteresis loop. The spin orbit transfer function in **(c)** shows the conversion of spin-to-charge. . . . 3

1.2 Ferroelectric spin-orbit logic (FESO) concept based on spin-textured ferroelectric stacks. . . . 4

1.3 **(a)** A ferromagnetic pillar (in grey) is patterned on top of a Pt nanostructure (in purple). A charge current I_c^{app} is applied to the nanomagnet (green arrow) in the x direction and it results in a spin current injection I_s along the z direction (yellow arrow) from the FM into Pt. The spin polarized current is converted into a charge current I_c^{ISHE} (red arrow) in the y direction by the ISHE in Pt, which results in a transversal charge accumulation that can be measured as a voltage (V_{ISHE}) in the open circuit condition. The portion of I_c^{app} that is not converted into I_s continues in the yellow electrode. **(b)** The plot shows the behavior of the signal $R_{ISHE} = V_{ISHE}/I^{app}$ as a function of the external magnetic field. . . . 5

1.4 **(a)** Schematic representation of the current in a F/N junction. The red and black arrows denote the conductivities for up and down spin electrons far from the interface. In the ferromagnetic material majority electrons experience less scattering events than minority, this leads to an higher majority current. **(b)** Electrochemical potential landscape at the F/N interface. Here, the red and blue lines represent the electrochemical potentials for the majority and minority spin populations. The transition from the ferromagnet to the non-magnet results in a spin current injection and a voltage drop at the interface V_{ac}, due to the spin accumulation. . . . 9

1.5 An illustration of every spin-dependent Hall effect. The spin up and spin down carriers are shown in red and blue. **(a)** In the AHE, a charge current flowing in a ferromagnetic material generates a polarized transverse charge current. **(b)** In the SHE, a charge current generates a transverse polarized pure spin current. **(c)** In the ISHE, a pure spin current generates a transverse charge current. As we can see every effect exhibit the same spatial symmetry. Adapted from [16]. 12

1.6 **(a)** Spin dependent skew scattering. Carriers with different spins (green and yellow colours) are deflected in the opposite way by the gradient in the relativistic magnetic field near an atom, the wave-vector is not conserved. **(b)** side-jump scattering, the wave-vector is conserved in this case. **(c)** Intrinsic SHE in which the spin dependent displacement is caused by asymmetries in the electronic band structure. 15

1.7 Intrinsic spin Hall conductivity calculated with tight binding for different $4d$ and $5d$ transition metals. Adapted from [28]. 16

1.8 Blue and red arrows indicate spin orientation for the two SOC-split bands at the Fermi level. The spin textures can be of three different types: Rashba,Dresselhaus, and PST. Adapted from [8]. 17

1.9 **(a)** The image shows the heavy metal (*e.g.* Pt or Ta) /nanomagnet (*e.g.* CoFeB or NiFe) stack and the distribution of the currents. When a charge current I_c^{app} is injected in the nanomagnet a spin accumulation builds at the interface with the non-magnet, that results in a spin current injection J_z^s. The inverse spin Hall effect in the SOC material converts the spin current into a trasversal charge current I_c^{ISHE}, this charge current will result in a build up of charge that can be measured as a trasversal voltage V_{ISHE} in the open circuit condition. 18

2.1 Vapour pressure as a function of temperature of commonly evaporated elements. 24

2.2 **(a)** The geometry and coordinate system used in modelling point source PVD systems. Here, a portion of the substrate surface A_k sits on the wafer holder at an angle θ_k with respect to the holder's normal and it's coated by the incoming material flux from an isotropic emitting point source. **(b)** A more realistic situation with a small planar source. In this case, the projected area of the source A_i^p as seen from the spot A_k on the substrate is taken into account. Adapted from [41]. 25

2.3 **(a)** is shown a situation where the sticking coefficient is close to 1 so the species are deposited where they first strike. **(b)** the sticking coefficient is much less then one which means that there's more diffusion and remission that leads to a more conformal film. 26

2.4 **(a)** Sketch of an e-beam evaporator. **(b)** Photograph of the *Evatec Bak 640* e-beam evaporator. A base pressure of $10^{-6} mBar$ is obtained by using cryogenic pump. It allows the deposition of multilayers using six crucibles, with an on-flight control of deposition rate and thickness through quartz microbalances. 27

2.5 The *Moorfield Minilab 080* is a compact standardized configuration for a thermal evaporation system that allows for multilayer deposition with fully automated process control. 28

2.6 Processes characterizing the cold plasma during sputtering. Accelerated Ar ion sputters a target atom (*e.g.* Al). The Al migrates to the wafer surface where it can: stay absorbed, diffuse to another surface site or be re-emitted. The Ar ion can be neutralized during sputtering and incorporated in the growing film, secondary electrons can be emitted by the target during sputter and they can: ionize an impurity that travels to the wafer surface or ionize Ar and sustain the plasma. 29

2.7 **(a)** Arrival angles distribution from a small or point like source as modelled in thermal systems. **(b)** Sputtering targets provide a wide range of arrival angles. Adapted from [41]. 30

2.8 **(a)** Sputtering tool sketch. Inside the vacuum chamber, a cold plasma of Argon is generated with an RF or DC field. The Argon ions in the plasma are accelerated to the target and they knock out atoms with their kinetic energy and momentum. **(b)** The *AJA ATC Orion 8* sputtering system is an integrated deposition tool which features DC or RF plasma operation, enabling sputtering of conductive or insulating materials. 30

2.9 **(a)** The *Heidelberg NanoFrazor Explore* is the first commercial t-SPL tool, with an hybrid direct laser sublimation and greyscale patterning capability in a single fabrication step. In-situ imaging enables two unique features: markerless overlay, and comparison of the written and target patterns during writing, so the parameters can be immediately adjusted. **(b)** A representative sketch of the NanoFrazor closed loop lithography concept which enables extreme vertical (indentation depth) and lateral resolution. 31

2.10 Overview of concepts of local modifications induced by a t-SPL on a sample. **(a)** Removal of material by thermomechanical indentation or sublimation of a sample material; **(b)** conversion of a sample by local modification of its physical properties such as the crystallinity or magnetic/ferroelectric dipole orientation, or chemical conversion; **(c)** addition of a functional material by melt transfer from a heated tip to the substrate or from a gas phase such as chemical vapor deposition of a precursor material. Adapted from [44]. 32

2.11 The figure shows the heat transfer from a heated cantilever and cantilever tip. Heat transfer from the heaters is mainly due to conduction within the cantilever and cantilever tip, and through the air near the cantilever. Heat transfer at the tip-substrate contact is mainly due to solid-solid contact, although the presence of water at the tip-substrate interface can also affect the heat transfer. Adapted from [49]. 37

2.12 Representation of the optical lithographic methods for positive and negative resists. For positive resist the exposed areas are removed during development, whereas in the other case the negative image of the mask remains. 38

2.13 In **(a)** the resist "overcut" due to attenuation of the light during its propagation in the resist is shown. The angles are close to 90° in reality. In **(b)** the resist "undercut" is shown, this profile allows for optimized lift-off and can be achieved by inverting the photoresist. 38

3.1 Complete device sketch with the heavy metal (in black) and the nanomagnet (in red). A current I_{in} is injected in the magnet which has a magnetization m in plane. The spin accumulation at the interface with the heavy metal leads to a spin-current injection (out of plane). The spin-current is converted in a trasversal charge current I_{ISHE} which leads to a charge accumulation that can be measured as a voltage V_{ISHE} in the open circuit condition. Additional transversal electrodes are contacted to measure the longitudinal resistivity of the heavy metal. 42

3.2 **(a)** Approach/retract curve; at point 1 the cantilever is moving towards the surface and so the reader voltage increases. Point 2 shows the so-called "snap-in" event. At point 3, the elastic restoring force of the cantilever is bigger than the adhesion force between the tip and the surface, and the tip "snaps-off". The difference in piezo extension between point 2 and point 3 is called the "adhesion length". At point 4 the cantilever's separation from the surface is controlled only by the z-piezo's position. **(b)** A pristine sharp tip with a short adhesion length (below 50 nm). 43
3.3 This picture shows a typical cantilever temperature curve calibration. . . . 45
3.4 Sudden jumps in the measured depth caused by loss of contact. Reducing the reading height typically helps. 46
3.5 The tip scans the surface at a constant write height. The value of this write height should be set so that, when the writer voltage is turned on, the thermal plus electrostatic deflections get the tip in contact with the surface. 47
3.6 When the write height is extremely low, the NanoFrazor writes all the scanned region instead of the target pattern even though the depth feedback has already set the force to the minimum (0 V). 48
3.7 The resulting patterning achieved after optimization of both the reading and writing parameters. The actual depth is equal to PPA thickness and there are no reading artifacts. 49
3.8 **(a)** A sketch of the layout with the different lithographic fields. **(b)** Reading mode image after patterning with the laser. **(c)** t-SPL field aligned with the optical ones. **(d)** Optical microscope image of the developed patterns. 51
3.9 **(a)** The NanoFrazor tip imprints a pattern by locally sublimating the thermal resist PPA. **(b)** The sample is developed in a solution and the pattern is transferred in the lift-off resist layer PMMA; wet isotropic processes lead to the so called "undercut". **(c)** A metallic thin film is deposited. **(d)** Finally, the sample is immersed in a proper solvent to strip the residual resist layers. As a result, the metallic pattern is formed on the substrate. . 52
3.10 The bilayer lift-off process is repeated. 52
3.11 **(a)** Nanofrazor's reading of a 50 nm line in which the depth profile recalls the conical shape of the tip; **(b)** larger PPA thicknesses result in a wider indentation. 53
3.12 **(a)** degraded PPA; **(b)** pristine PPA. 54
3.13 **(a)** Optimal development (no residual PMMA/MA); **(b)** under-developed sample. 54

3.14 Development rate test done by *Heidelberg Instruments* on a PPA (30)/PPMA (270) stack. 55
3.15 **(a)** a weak point in the structure that can lead to resist collapse. **(b)** an example of a bad lift-off. 56
3.16 Optimization of the thickness of the PMMA/MA layer. The points indicate the mean. 57
3.17 NanoFrazor *in-situ* reading of the t-SPL patterning.**(b)** The structure after lift-off.**(c)** Optical microscope image of the device after this step. 58
3.18 The Nanofrazor's reading and writing procedure allows to align the magnetic pillar on top of Pt exactly in the desired position and without any markers. 59
3.19 **(a)** SEM image of the finalized nanostructure, **(b)** higher magnification image. 60
3.20 **(a)** Optical microscope image of the finalized device complete with evaporated noble metal output contacts; **(b)** higher magnification image. 60

Acknowledgements

I want to thank Christian Rinaldi, Federico Fagiani, Luca Nessi, Matteo Cantoni and everyone I worked with at Polifab, for the experience I acquired in the making of this thesis. Moreover, I'm grateful to my parents that made possible for me to reach this goal.